2017

Geometric Influence on Electronic Properties: Graphene with Antidots, Two-Dimensional Electron Gas and Three-Dimensional Carbon Nanostructures

Lei Wang
University of South Carolina

GEOMETRIC INFLUENCE ON ELECTRONIC PROPERTIES: GRAPHENE WITH ANTIDOTS, TWO-DIMENSIONAL ELECTRON GAS AND THREE-DIMENSIONAL CARBON NANOSTRUCTURES

by

Lei Wang

Bachelor of Science
Shandong University of Science and Technology, 2008

Master of Science
Chinese Academy of Sciences, 2011

Submitted in Partial Fulfillment of the Requirements

For the Degree of Doctor of Philosophy in

Physics

College of Arts and Sciences

University of South Carolina

2017

Accepted by:

Timir Datta, Major Professor

Richard Creswick, Committee Member

Milind Kunchur, Committee Member

Richard Adams, Committee Member

Ming Yin, Committee Member

Cheryl L. Addy, Vice Provost and Dean of the Graduate School

DEDICATION

Dedicated to my beloved family for their endless support and encouragement.

ACKNOWLEDGEMENTS

First, I want to thank my advisor Dr. Timir Datta for his endless support and help on my study and life. Dr. Datta is always full of patience, energy and wisdom. He keeps reminding me to be creative. I can always learn new things when we discuss the experiment and data. My written English has been improved a lot and I learned how to express myself clearly during manuscript revision. Furthermore, he cares about my life, just like my daddy. We went to beach together to enjoy the break. He told me how to get along with people and assimilate into American culture, how to deal with trouble in life.

Second, I started the cooperation with Dr. Ming Yin since 2012. We traveled to National High Magnetic Field Laboratory several times together with his funding. He is always glad to help me to set up the equipment, fill the helium and take data. I really enjoy the collaboration with him. I cannot finish my thesis without his generous support.

Third, I would love to thank my committee members. Dr. Richard Creswick as graduate director gave me a lot of help for the recommendation letters and application for travel grants of Graduate School. I really appreciate his careful revision and constructive suggestions on my PhD thesis. The thin film course offered by Dr. Milind Kunchur is very useful for my research. Really appreciate Dr. Richard Adams from Chemistry Department for useful suggestion and criticism for my thesis.

Then, special thanks go to Dr. Richard Webb, Dr. Thomas Crawford, Dr. Bochen Zhong, Ning Lu and Heath Smith for the help of graphene nanostructure fabrication. Thank Dr. Asif Khan, Sakib Muhtadi, Dr. Fatima Asif and Antown Coleman in Electrical Engineering Department for the help of AlInN/GaN device fabrication.

I got a lot of help from Dr. Jan Jaroszynski, Dr. Eun Sang Choi and Dr. Ju-Hyun Park when I conducted measurements at the National High Magnetic field Laboratory, Tallahassee FL. I really appreciate your assistance and useful discussion.

To my best friend, Dr. Dawei Li, we experienced a lot. To Katia Gasperi, Nahid Shayesteh Moghaddam, Lin Li, Tongtong Cao and Hao Jiang, you guys are awesome and I don’t think I could make it without your help and encouragement.

Finally, my family is a constant power source for my growth and accomplishment of PhD degree. Thank you for the endless support.

ABSTRACT

Geometric influence on electrical and magneto transport properties has been investigated in three types of systems: (i) Graphene, a single layer of carbon atoms; (ii) Two-dimensional electron gas (2DEG) in AlInN/GaN heterostructure; and (iii) 3D carbon nanostructures, a special type of three-dimensional materials with spherical voids. Due to unique structures and energy dispersion relations, these three systems demonstrate distinct physical properties.

AlInN is the newest and amongst the widest band gap semiconductors. The 2DEG in AlInN/GaN heterostucture displays long transport lifetime along with conventional behaviors, including Shubnikov-de Haas (SdH) oscillation and weak localization. From SdH oscillation, the effective mass of electron is obtained as $0.2327m_e$. We report the first observation of weak localization in this heterostructure. Electron-electron scattering is the principal phase breaking mechanism in this system.

In contrast, graphene has an unconventional linear energy dispersion relation near the Dirac points. We determine the effective mass of electron is $0.087m_e$ in CVD graphene, much smaller than that in 2DEG. In addition, due to pseudo spin and nonzero Berry phase, weak localization in graphene is more complex. Furthermore, the introduction of an antidot lattice has great influence on transport in graphene. We demonstrate that the carrier density and effective mass can be controlled by such manipulation. By tuning

antidot size, a band gap ~ 10 *meV* is obtained. Geometric control of the band gap is likely to promote electronic applications of graphene.

As observed in graphene and the 2DEG, the magneto response is typically sensitive to the orientation between the applied magnetic field and input current. However, we demonstrate that orientation independent response and linear magnetoresistance can be achieved in three-dimensional carbon nanostructures with spherical voids. With the increasing void size, the linear magnetoresistance is enhanced and a metal to insulator transition is observed. The combination of orientation insensitivity and linear magnetoresistance is very useful for magnetic field detectors, particularly at high magnetic fields.

TABLE OF CONTENTS

LIST OF TABLES

LIST OF FIGURES

LIST OF SYMBOLS

R	Resistance.
T	Temperature.
B	Magnetic field.
n	Carrier density.
e	Charge of electron.
u	Carrier mobility.
h	Planck constant.
$\hbar$	Reduced Planck constant.
k_B	Boltzmann constant.
m^*	Effective mass of carrier.
E_F	Fermi enery.
v_F	Fermi velocity.
E_C	Minimum energy of conduction band.
E_V	Maximum energy of valance band.
$E(\vec{k})$	Energy as a function of wavevector $\vec{k}$.
$\hat{H}$	Hamiltonian.
$\hat{p}$	Momentum operator. $\vec{p}$ is momentum.
D	Diffusion constant.
n_L	Landau index.
g_s	Degeneracy.

ω_c Cyclotron frequency.

τ Relaxation time. τ_e is elastic scattering time, τ_{in} is inelastic scattering time, τ_t is transport lifetime, τ_q is quantum lifetime, τ_i is intervally scattering time.

LIST OF ABBREVIATIONS

AlInN ..... Aluminum Indium Nitride

BZ ..... Brillouin Zone

GaN ..... Gallium Nitride

MR ..... Magnetoresistance

SdH ..... Shubnikov de Haas

2DEG ..... Two Dimensional Electron Gas

WL ..... Weak Localization

CHAPTER 1

INTRODUCTION

With the development of the semiconductor industry, the physical feature size of devices keeps decreasing. The width of the gate in transistors has already reached below 10 *nm*. In order to continue Moore's law in semiconductor industry, new materials are needed. So far, a variety of alternative materials have been predicted to replace silicon. These new materials include graphene [1-3], nitride based compounds [4-6], Weyl semimetals [7,8] and topological insulators [9,10]. No matter what the material is, high mobility and high carrier density are critical for device performance. In order to improve carrier mobility, scattering processes have to be understood and suppressed. Transport measurements are effective tools for elucidating scattering mechanisms and they also provide information about Fermi energy, effective mass and coherence length.

When the feature size of a device is decreased to a few nanometers, quantum effects become prominent. According to the Uncertainty Principle

$$\Delta x \, \Delta p \geq \frac{\hbar}{2} \tag{1.1}$$

Here Δx and Δp is the uncertainty of position and momentum of carriers respectively, $\hbar = h/2\pi$ is the reduced Planck constant. The position and momentum of a particle cannot be simultaneously measured with arbitrarily high precision. When the size is

decreased to a few nanometers, the fluctuations in the momentum become very large. Hence the wave nature of carrier is prominent. Quantum effects will dominate the properties of system. Consequently many traditional techniques to tune the properties of materials may fail. For example, chemical doping is widely used to change the carrier density and band gap in silicon, but when the size of device is decreased to nanometers, chemical doping may not be effective anymore. The lattice constant of silicon crystal is 5.4 Angstrom. The doping concentration of silicon typically ranges from $10^{13}\,cm^{-3}$ to 10^{18} cm^{-3}. That means there are approximately 8×10^{21} silicon atoms in 1 cm^3 crystal. Thus 10 000 silicon atoms share one dopant atom. This chemical doping works well when the size of devices is large. But when the devices are reduced to a few nanometers, which have only tens of silicon atoms, how can we dope each device? Some devices may have a dopant, whereas some may not if we keep the same doping level. It is hard to realize the homogeneous doping in every region down to nanometers. If we increase the doping concentration, the chemical elements may introduce extra scatterings. Hence new methods to tune the electronic properties become necessary, especially in graphene. As we all know, graphene, a single layer of carbon atoms, has many novel properties, such as exceptional strength, thermal conductivity and electrical conductivity. But graphene is a semimetal with zero band gap [11], which limits its potential application in electronics. One effective technique to modify the electrical properties of graphene and to open a band gap is the introduction of nanoribbon [12,13] and antidots [14,15]. An antidot lattice is a regular array of holes, which is the opposite of dots. We remove the atoms and make holes on the materials.

In this thesis three materials, graphene with an antidot lattice, the two-dimensional electron gas in AlInN/GaN heterostructures and three-dimensional carbon nanostructures with voids, have been investigated. The electronic and magneto transport measurements, the scattering mechanism, effective mass of carriers, and carrier density and mobility were studied. Furthermore, we investigate the geometric influences of artificial structures such as antidots in graphene and spherical voids in three-dimensional carbon nanostructures.

1.1 TRANSPORT THEORY

Figure 1.1 shows the schematic diagram of transport and Hall measurement of carriers in a magnetic field. An input current *I* is applied to the sample in x direction, with the magnetic field *B* perpendicular to the sample in z direction $\vec{B} = (0, 0, B)$. When the sample is placed in a magnetic field, the Lorentz force $\vec{F}_L = q\vec{v} \times \vec{B}$ acts on the carrier with the charge *q*, so that the carrier moves to the side wall instead of straight motion. We can measure the longitudinal voltage V_x and Hall voltage V_H. According to the classical theory, the drift velocity $\vec{v}$ of carrier follows

$$m^* \frac{d\vec{v}}{dt} = -e\left(\vec{E} + \vec{v} \times \vec{B}\right) - \frac{m^*\vec{v}}{\tau} \tag{1.2}$$

Here $\vec{E} = (E_x, E_{y,}0)$ is the electric field. τ is the relaxation time, $m^*$is the effective mass of the carrier and e is the charge of electron. In the steady state $\frac{dv_x}{dt} = 0, \frac{dv_y}{dt} = 0$, we can solve v_x and v_y and the current density $\vec{\boldsymbol{j}}$.

$$\vec{\boldsymbol{j}} = \sigma\vec{E}$$

$$\sigma = \begin{pmatrix} \sigma_{xx} & \sigma_{yx} \\ \sigma_{xy} & \sigma_{yy} \end{pmatrix} \tag{1.3}$$

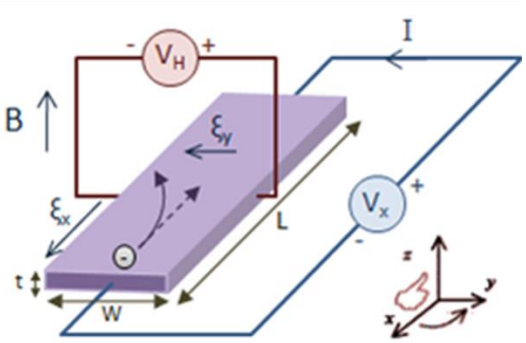

Figure 1.1 Transport measurement. The electron executes the cyclotron motion in the magnetic field due to Lorentz force, resulting in a Hall voltage.

The zero-field conductivity is

$$\sigma_{xx} = ne\mu = \frac{ne^2\tau}{m^*} \tag{1.4}$$

Here n is the carrier density, μ is the mobility, e is the charge of electron.

The Hall voltage measured perpendicular to current is

$$V_H = \frac{I_x B}{nte} \tag{1.5}$$

Here I_x is the input current; t is the thickness of sample. From the Hall measurement, the carrier density can be obtained. Combined with conductivity, the mobility is also available.

In the previous model, we didn't consider the energy band of system and neglect interactions with ions and other electrons. Figure 1.2 shows the energy structure in one dimension of a free electron and the electron in a crystal. For a free electron, the energy is a parabolic function of the momentum, $\mathrm{E(k)} = \frac{(\hbar \mathrm{k})^2}{2\mathrm{m}}$. The electron can occupy any state,

with any energy. But when the electrons are confined in a periodic potential in a crystal, the energy structure is modified. We can get the eigenenergies by solving the Schrödinger equation. Some energy levels are allowed, named valance band or conduction band. However, there is no eigenenergy at a certain value; that means the occupancy of electron in this level is forbidden. At the boundary of the first Brillouin zone, a gap is clearly seen in Fig. 1.2(b). Hence due to the periodic potential of crystal, the parabolic band structure is modified, with the forbidden gap and energy band. But for the region far away from the Brillouin zone boundary we can still simplify the dispersion relation as $E(k) = \frac{(\hbar k)^2}{2m^*}$, Here the mass of carrier has been changed to the effective mass m^*, which contains the information of crystal.

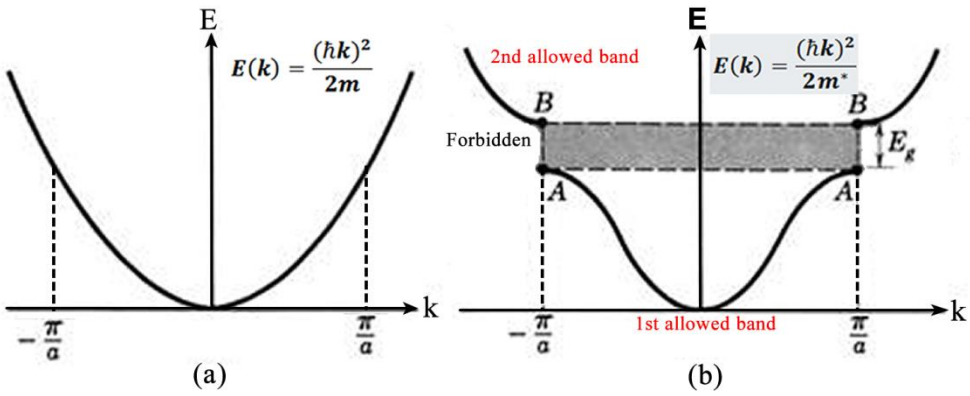

Figure 1.2 Energy v.s. momentum diagram. (a) Free electron. (b) Electron in a crystal.

When the material is placed in the electric field, the velocity of a carrier is determined by the energy band $\varepsilon(\vec{k})$ [16]. The velocity is

$$\vec{v}(\vec{k}) = \frac{1}{\hbar}\frac{\partial \varepsilon(\vec{k})}{\partial \vec{k}} \tag{1.6}$$

According to semi classical theory, the current density in a system is

$$\vec{J} = -\frac{2e}{(2\pi)^3}\int \vec{v}(\vec{k}) f(\vec{r},\vec{k},t)d\vec{k} \tag{1.7}$$

Where $f(\vec{r},\vec{k},t)$ is the non-equilibrium distribution function which determines the probability of finding an electron at position $\vec{r}$, crystal momentum $\vec{k}$ and time t. If there is no temperature gradient and no external electrical or magnetic field, the distribution function can be reduced to equilibrium distribution function, i.e. Fermi function $f_0(\varepsilon) = \frac{1}{e^{(\varepsilon-\mu)/k_BT}+1}$.

The distribution function$f\left(\vec{r},\vec{k},t\right)$ meets the following Boltzmann Equation

$$\frac{\partial f}{\partial t} + \vec{v}\left(\vec{k}\right)\frac{\partial f}{\partial \vec{r}} + \dot{\vec{k}}\frac{\partial f}{\partial \vec{k}} = \left(\frac{\partial f}{\partial t}\right)_{collision} \tag{1.8}$$

The seconder term is due to diffusion process, the third term is arising from external forces and fields.

Boltzmann equation is usually solved by two approximations:

(1) Linearization. When external fields and forces are sufficiently weak, the distribution function can be considered as the sum of its equilibrium function (Fermi function) plus a small term

$$f\left(\vec{r},\vec{k}\right) = f_0\left(\varepsilon(\vec{k})\right) + f_1\left(\vec{r},\vec{k}\right) \tag{1.9}$$

(2) Relaxation time approximation.

$$\left(\frac{\partial f}{\partial t}\right)_{collision} = -\frac{f-f_0}{\tau} = -\frac{f_1}{\tau} \tag{1.10}$$

Where τ denotes the relaxation time which characterizes the rate of return to the equilibrium distribution when the external fields or thermal gradients are removed and in general depends on crystal momentum, i.e. $\tau = \tau(\vec{k})$.

The overall relaxation time is determined by several different mechanisms: electron-electron scattering, τ_{e-e}, electron-phonon scattering, τ_{e-phon}, impurity and defect scattering, τ_{e-imp}, and other scatterings, so that

$$\frac{1}{\tau} = \frac{1}{\tau_{e-e}} + \frac{1}{\tau_{e-phon}} + \frac{1}{\tau_{e-imp}} + \cdots \tag{1.11}$$

The phonon, a quantum quasi-particle, is the quantum of vibrational motion of the atoms around their equilibrium positions [17]. Due to the vibration of the crystal lattice, an electron is easily scattered by phonons. Hence electron-phonon scattering plays an important role in the transport.

Electrons can also scatter off each other due to the Coulomb interaction. In solid state physics we usually use free electron approximation, where the periodic potential of the fixed lattice particles and of all the other electrons is replaced by an almost time-independent potential in order to describe the independent motion of a single conduction electron. There are, however, cases where the Coulomb interaction cannot be neglected such as in weak localization effect.

The current density can be calculated using equation 1.7 if $\vec{v}(\vec{k})$ and $f(\vec{r}, \vec{k}, t)$ are known. The velocity can be easily obtained if we know the energy band structure. On the other hand, the geometric structure of the system determines the energy band, which results in distinct and rich transport properties in various materials. So from the transport

measurement, we can also obtain the information about the band structure. In next sections, the two-dimensional electron gas in heterostructure and graphene have been discussed in detail.

1.2 AlInN/GaN HETEROSTRUCTURE

Gallium Nitride (GaN) based semiconductors have attracted much attention due to their potential application in high power and high frequency electronics. III-V semiconductors usually have a very large band gap. For example, GaN has a band gap ~ 3.4 eV and AlN ~ 6 eV, which is much larger than that of Si (~ 1.1 eV) and the energy of visible light as shown in Fig. 1.3. The electronic properties of compound semiconductors, such as band gap, mobility and carrier density, are controllable by tuning element composition, thickness and the growth condition of each layer. Furthermore, in contrast to graphene and other 2D materials, the existing techniques of silicon can easily be applied on III-V semiconductors without much change.

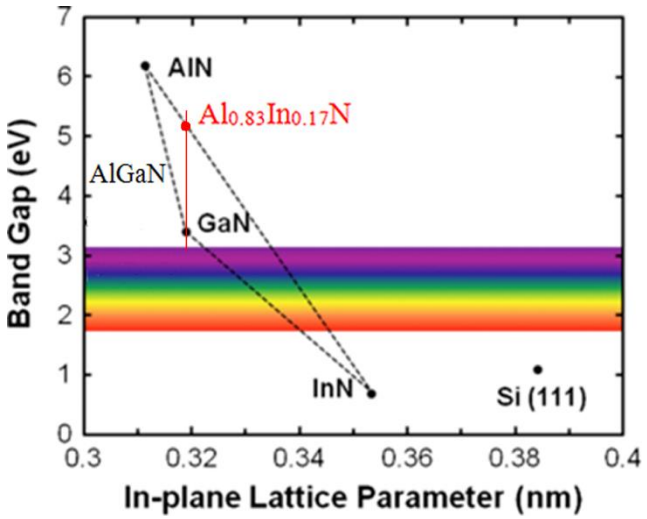

Figure 1.3 Band gap and lattice constant for several semiconductors. The color band represents the spectrum of visible light.

First, let us discuss the band diagram of heterostructure. A heterostructure is a junction which is made by two different semiconductor materials. For example, Fig. 1.4 shows the band structure of n-doped AlGaAs and intrinsic GaAs [18]. E_C is the minimum energy of conduction band, E_V is the maximum valance band energy, E_F is the Fermi energy. The band gap is defined as $E_g = E_C - E_V$. Clearly, AlGaAs has a much larger band gap than that of GaAs. Before these two materials are brought together to form a heterostructure, the Fermi energy of AlGaAs is higher than that of GaAs. When these two materials are brought into contact with each other, electrons in AlGaAs have higher energy and can move to unoccupied levels in GaAs. When the electron density of AlGaAs decreases, E_F decreases as well. The transfer of carriers will stop when the Fermi energies E_F of the two materials are equal. The redistribution of charge forms an electrostatic potential at the interface between AlGaAs and GaAs and electrons are confined in this well. The two-dimensional electron gas (2DEG) is shown in Fig. 1.4; the conduction band of GaAs near the interface is bent down due to electron accumulation [19].

Recently, the AlInN/GaN heterostructure has attracted a great deal of interest. In contrast to the AlGaN/GaN system, with AlInN as the barrier one can achieve lattice matching to GaN by tuning the composition between AlN and InN. When In is set to ~ 18%, the AlInN and GaN lattice is matched, as shown in Fig. 1.3. This will greatly increase the crystal quality and carrier mobility. Moreover, the band gap of $Al_{0.83}In_{0.17}N$ is also very large, ~ 5eV.

The band diagram of $Al_{0.83}In_{0.17}N$/AlN/GaN heterostructure, obtained from a one dimensional self-consistent Schrodinger-Poisson equations solver [20] is shown in Fig.

1.5. In order to get a high quality AlInN layer, a very thin (~1 nm) AlN is deposited first. We can clearly see the potential well around 4 nm; the red peak shows very high carrier density, indicating the confinement of two-dimensional electron gas.

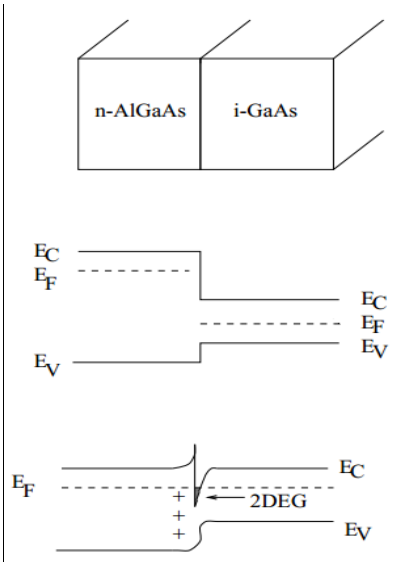

Figure 1.4 Band diagram of the interface between n-doped AlGaAs and intrinsic GaAs [18]. The middle is the diagram before charge transfer. Bottom is the situation in equilibrium.

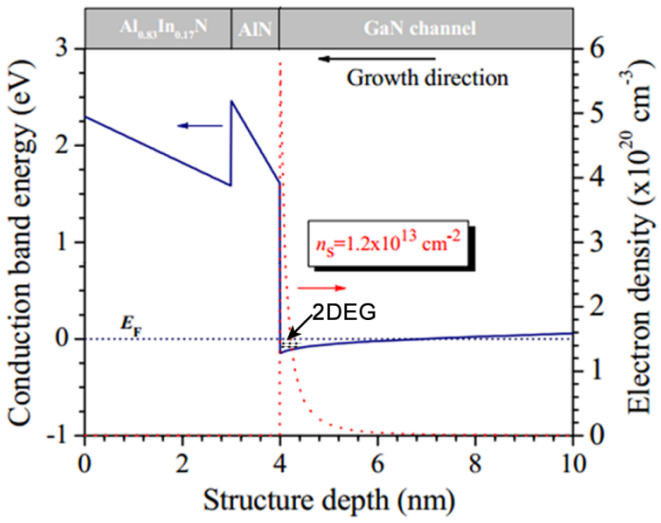

Figure 1.5 Band diagram and the 2DEG distribution along the growth direction for the $Al_{0.83}In_{0.17}N$/AlN/GaN heterostructure [20].

However, for the AlInN/GaN heterostructure, GaN and AlInN are both undoped. Where does the two-dimensional electron gas (2DEG) come from?

Charge polarization is a significant property of the III-V nitride semiconductors [21]. Due to the difference in the ionicity of the two atoms, the bonds in all III-V or II-VI compound semiconductors are polar. There are two types of polarizations, spontaneous and piezoelectric polarization. The piezoelectric polarization is produced due to the lattice mismatch. The condition for spontaneous polarization is the *c/a* ratio must differ from the ideal ratio of $\sqrt{8/3}$ [22].

GaN and AlN are wurtzite crystal systems. The lattice constant *a* is the edge length of basal plane, and *c* is unit cell height. All the nitrides have lower *c/a* ratio than ideal, which is necessary for stability. The magnitude of the spontaneous polarization of GaN is around 0.034 C/m^2, but in AlN it is much bigger, ~0.09 C/m^2, the largest value in all nitrides because of the largest deviation from the ideal *c/a* ratio. Polarization induces surface charges, shown in Fig. 1.6. An electric field is induced owing to the surface charges, which leads to the tilt of band structure. Clearly, the band structures of AlInN and AlN in Fig. 1.5 are both tilted.

The formation of 2DEG at the interface arises from the existence of donor states on the AlInN surface [21]. An electron in a surface state can be excited to the conduction band of AlInN with the help of induced electric field by surface charge, where it will flow to the GaN side and accumulate at the interface to form the 2DEG. The carrier density can be changed by adjusting the thickness of the AlInN barrier. Hence the spontaneously

polarized 2DEG can be realized without doping, which greatly reduces the scattering from impurities.

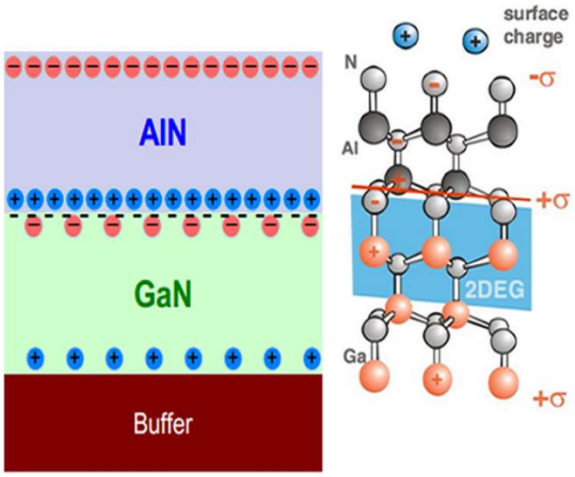

Figure 1.6 Polarization and surface charge of GaN and AlN.

1.3 LANDAU LEVEL AND SHUBNIKOV-DE HAAS OSCILLATION

Classically, a free electron executes a circular motion in a perpendicular magnetic field due to the Lorentz force $\vec{F} = -e\vec{v} \times \vec{B}$. The cyclotron frequency is $\omega_c = eB/m$. In the quantum mechanics, we need to solve the Schrödinger equation.

$$\hat{H}\Psi = E\Psi \tag{1.12}$$

Here Ψ is the electronic wave function. The Hamiltonian is $\hat{H} = \frac{1}{2m}(\hat{P} - q\vec{A})^2$. Where $\vec{P}$ is the momentum operator and $\vec{A}$ is the vector potential which is related to the magnetic field by $\vec{B} = \nabla \times \vec{A}$.

For simplicity, the Landau gauge is used $\vec{A} = \begin{pmatrix} 0 \\ Bx \\ 0 \end{pmatrix}$. Then the Hamiltonian becomes

$$\hat{H} = \frac{\hat{p}_x^2}{2m} + \frac{1}{2m}(\hat{p}_y - qB\hat{x})^2 \tag{1.13}$$

Solving this Schrödinger equation will give the eigenenergy. In fact, this is same to the Harmonic oscillation. So the energies are

$$E_n = (n_L + 1/2)\hbar\omega_c. \tag{1.14}$$

Here n_L=0, 1, 2, 3…; $\hbar$ is the reduced Planck constant, $\omega_c = eB/m^*$ is the cyclotron frequency. e is the electron charge and m^* is the effective mass of carriers. In quantum mechanics, the magnetic flux is quantized and the band structure becomes quantized Landau level. The Landau energy E_n is linearly proportional to magnetic field B and index n_L. The space between each Landau level is equal, as shown in Fig. 1.7(a).

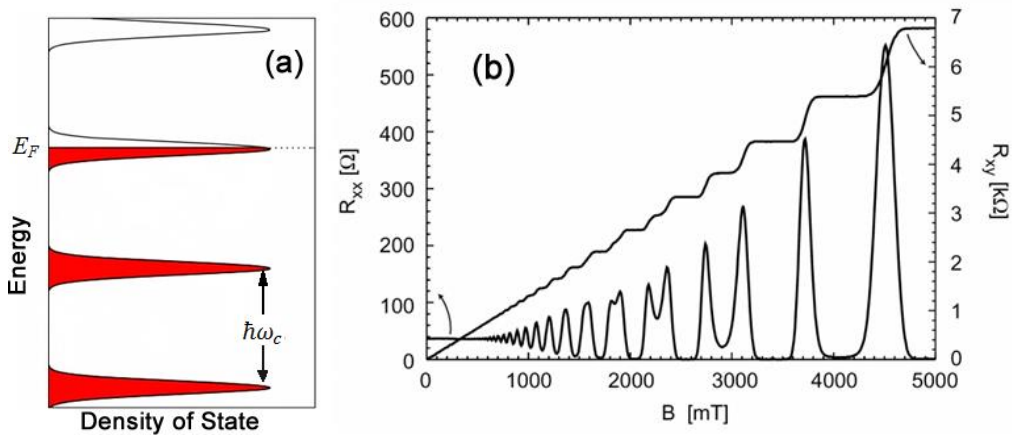

Figure 1.7 (a) Landau levels. E_F is the Fermi energy. (b) Shubinikov de Haas oscillation and Quantum Hall effect.

For each Landau level, the degeneracy in unit area is $N = \frac{g_s B}{\emptyset_0} = \frac{g_s Be}{2\pi\hbar}$. Here g_s represents a factor of 2 due to spin degeneracy for conventional 2DEG. For graphene, $g_s = 2 \times 2 = 4$ because of double spin and double valley degeneracy. The degeneracy is proportional to magnetic field. When magnetic field is increased, the degeneracy is also increased. That means there are more states in each Landau level and more carriers can occupy the same Landau level.

For a system, the charge carrier density is constant at a certain temperature. Since each state can only have 2 carriers due to spin degeneracy, the number of filled states below Fermi energy E_F is also constant. When the magnetic field B is increased, the degeneracy for each Landau level will be also increased. Hence the Fermi level E_F will drop to lower value with increasing magnetic field B. When E_F passes through a Landau level from higher energy, the measured resistance oscillates periodically. This is called Shubnikov-de Haas (SdH) oscillation.

It is important to know that at high magnetic fields, the carriers in the interior region execute cyclotron motion. But at the boundaries, orbital motion is disrupted and the carriers get scattered forward along the edge leading to a large conductance. When the Fermi energy is between two Landau levels, the edge state related carriers dominate the conduction, so the resistance is very small which corresponds to the minima in the longitudinal resistance R_{xx} in Fig. 1.7(b). When the Fermi energy moves to inside of Landau level, the scatterings due to interior carriers become strong and result in a high resistance.

In fact, SdH oscillation is a periodic function of *1/B*, instead of magnetic field *B*. And the frequency B_F is directly proportional to carrier density $n_{SdH} = g_s eB_F/(2\pi\hbar)$. So the carrier density can be obtained by the SdH oscillation without measuring the Hall voltage.

The amplitude of SdH oscillation can be expressed by

$$\Delta R_{xx} = 4R_0 \frac{\chi}{\sinh(\chi)} \exp(\frac{-\pi}{\omega_c \tau_q}) \tag{1.15}$$

Here $\chi = 2\pi^2 k_B T/\Delta E$ and the Landau level energy spacing $\Delta E = \hbar\omega_c = \hbar eB/m^*$. $k_B$is the Boltzmann constant, $\hbar$ is the Planck constant, e is the electron charge and $\tau_q$is the quantum lifetime. The temperature dependent SdH oscillation is useful to analyze the Fermi surface, effective mass $m^*$and quantum scattering mechanism.

1.4 GRAPHENE

Graphene is made of a single layer of carbon atoms, with a hexagonal lattice structure as shown in Fig. 1.8(a). Atom A (red) and atom B (blue) are inequivalent, so the graphene structure can be viewed as a triangular lattice with a basis of two atoms A and B.

The Bravais lattice vectors are [11]

$$\vec{a}_1 = \frac{a}{2}(3, \sqrt{3}), \vec{a}_2 = \frac{a}{2}(3, -\sqrt{3}) \tag{1.16}$$

Where a ~1.42 Å is the nearest carbon to carbon distance.

The reciprocal lattice vectors are

$$\vec{b}_1 = \frac{2\pi}{3a}(1, \sqrt{3}), \vec{b}_2 = \frac{2\pi}{3a}(1, -\sqrt{3}) \tag{1.17}$$

so the first Brillouin zone can be drawn and it is hexagonal as shown in Fig. 1.8(b).

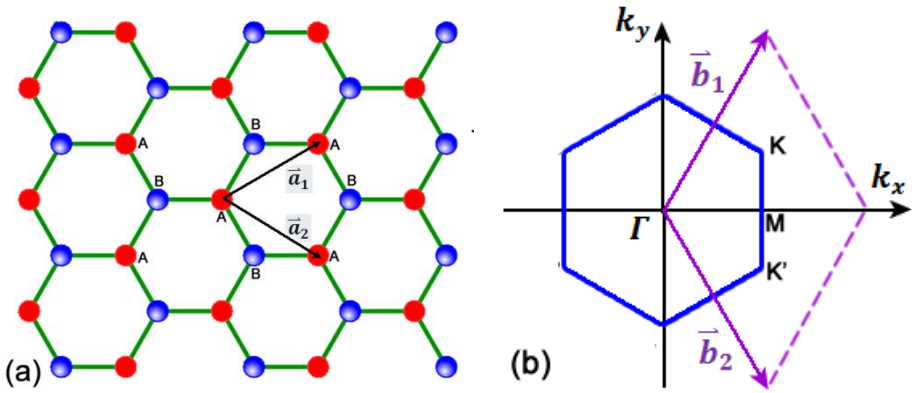

Figure 1.8 (a) Honeycomb lattice of graphene, with two types of atoms A and B. $\vec{a}_1$ and $\vec{a}_2$ are lattice vectors. (b) The reciprocal lattice vectors and the 1st Brillouin zone [11].

For each carbon atom, there are four valence electrons. Three electrons form the chemical bonds in the plane, named σ bonds. These three σ bonds are localized and cannot contribute to the electronic conduction. The $2p_z$ orbital is oriented perpendicular to the plane, which is free to move, and forms the π band.

The energy bands derived using the nearest neighbor tight-binding method are [11,23]

$$E(\vec{k}) = \pm t\sqrt{3 + 2\cos\left(\sqrt{3}k_y a\right) + 4\cos\left(\tfrac{\sqrt{3}}{2}k_y a\right)\cos\left(\tfrac{3}{2}k_x a\right)} \qquad (1.18)$$

Here t is the nearest neighbor hopping energy. The energy band is plotted in Fig. 1.9. $E < 0$ is the valence band, $E > 0$ is conduction band. The two bands touch each other at the six corners (Dirac points). The gap in graphene vanishes and graphene is not a semiconductor. Moreover since each carbon atom contributes a single electron, the

negative energy band is fully filled while the positive band is empty (electron - hole symmetry). The Fermi energy is $E_F = 0$ at zero temperature.

The positions of Dirac points K and K' shown in Fig. 1.8(b) in momentum space are given by [11]

$$\boldsymbol{K} = \frac{2\pi}{3a}\left(1, \frac{1}{\sqrt{3}}\right), \ \boldsymbol{K'} = \frac{2\pi}{3a}\left(1, -\frac{1}{\sqrt{3}}\right) \tag{1.19}$$

For the region near K and K', the energy dispersion, if we only take the first order, can be expanded as [11,23]

$$E(\vec{k}) \approx \pm \hbar v_F \left|\vec{k}\right| \tag{1.20}$$

The energy surface is plotted in Fig. 1.9 and consists of two circular cones touching each other at $E = 0$. Furthermore, this is very similar to the linear dispersion relation of photons where the speed of light c is replaced by the Fermi velocity v_F. For graphene, $v_F = 3ta/2 \sim 10^6 m/s$ [11], very large speed compared to the conventional 2DEG, so the carriers at the Dirac points in graphene behavior like massless particles.

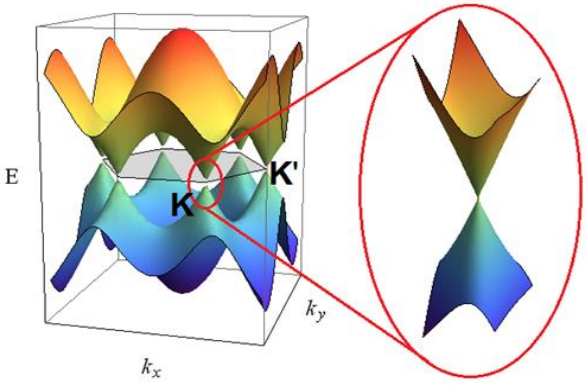

Figure 1.9 Energy band derived from the nearest-neighbor tight binding model [24]. Zoomed in figure is the band structure around Dirac points K.

When the graphene is placed in the magnetic field *B*, the energy is also quantized to Landau levels. Unlike the conventional 2DEG, the Landau levels of graphene in a magnetic field are [11,25]

$$E_n = \pm v_F \sqrt{2e\hbar B n_L} \tag{1.21}$$

Here the Landau index n_L= 0, 1, 2,…, *e* is the charge of electron, $\hbar$ is the reduced Planck constant. $\pm$ is the band index and refers to the conduction (electrons) / valence (holes) band. The Landau level is proportional to the square root of magnetic field *B* and index n_L, unlike the linear relation of massive quasi-particles $E_n = \left(n_L + \frac{1}{2}\right)\hbar\omega_c$. The gaps between Landau levels in graphene are not equal, as shown in Fig. 1.10. Remarkably, there exists a zero-energy Landau level in graphene when n_L=0 and it is independent on the magnetic field [25].

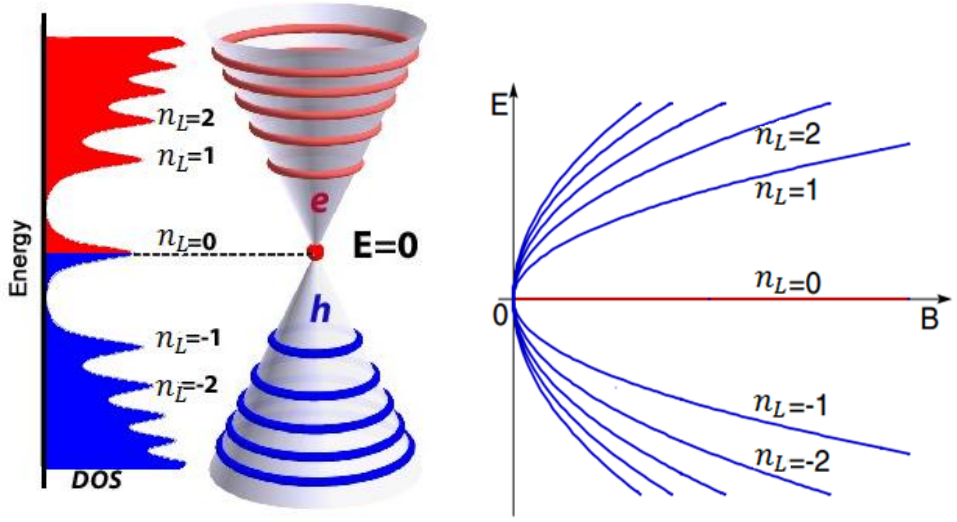

Figure 1.10 Landau level in the magnetic field. Each level is not equally spaced; instead it is proportional to square root of *B* [25].

1.5 WEAK LOCALIZATION

At low temperatures phonon scattering is suppressed, which induces a long mean free path and coherence length. So the wavelike nature of charge carriers at low temperature becomes important. In this regime, due to constructive quantum interference, the carrier has an enhanced probability to be scattered back to the origin along a closed loop in opposite directions, resulting in a larger resistivity compared to the Drude model. This is called weak localization and widely observed in disordered systems [26,27].

The probability for a carrier propagating from point A to B, as shown in Fig. 1.11(a), is the sum of all the Feynman's paths between A and B [18]

$$P = |\sum_i A_i|^2 = \sum_i |A_i|^2 + \sum_{i \neq j} A_i A_j^* \tag{1.22}$$

Here $A_j = |A_j| e^{i\varphi_j} = |A_j| e^{i\vec{k}_j \vec{l}_j}$ is the propagation amplitude along path j. The first term is the classical probability, and second term is interference part. For each path the carrier experiences diffusive motion like a random walk. Because the scattering is elastic, the phase acquired along any path is well defined, but different along each Feynman path. When averaged over a large number of paths, the interference term vanishes.

However, there is a special case. For self-crossing trajectories, just like point O as shown in Fig. 1.11(b), the electron can be scattered along clockwise or counterclockwise back to the origin O. The phases $\Delta\varphi$ acquired in these two directions are exactly same, because the propagation $\vec{p} \rightarrow -\vec{p}$, $d\vec{l} \rightarrow -d\vec{l}$. It can be viewed as a motion of a carrier and its time-reversed counterpart. Hence this constructive interference has time reversal symmetry. The probability for a closed path at point O is

$$\left|A_{+p}+A_{-p}\right|^2=\left|A_{+p}\right|^2+\left|A_{-p}\right|^2+2A_{+p}A^*_{-p}$$

$$=\left|A_{+p}\right|^2+\left|A_{-p}\right|^2+2\left|A_{+p}\right|e^{i(\varphi+\Delta\varphi)}\left|A_{-p}\right|e^{-i(\varphi+\Delta\varphi)}=4\left|A_p\right|^2 \quad (1.23)$$

Here$\left|A_{+p}\right|$=$\left|A_{-p}\right|$. The probability of a carrier to be scattered back to the origin is 4 times as large as the classical value. This coherent back-scattering leads to an increase in resistance compared with the classical Drude model. The condition for weak localization to occur is that the phase coherence length should be much longer than the mean free path so that the carrier can return to the origin after several times of scattering [27].

Weak localization can be suppressed at high temperature. Inelastic scattering such as a collision with a phonon or another electron can change the momentum of the carrier which destroys the phase coherence. When the temperature is increased, scattering becomes strong and the coherence length is reduced. So the effect of weak localization becomes weak.

The application of a magnetic field can also affect the weak localization, because the magnetic field breaks the time reversal symmetry and destroys the interference. Hence with increasing magnetic field, the probability of back scattering is decreased, which leads to an increase in the magnetoconductivity. The change of magnetoconductivity [5,28,29] is

$$\Delta\sigma_{xx}=\sigma_{xx}(B)-\sigma_{xx}(0)=\frac{e^2}{\pi h}\left[\psi\left(\frac{1}{2}+\frac{\hbar}{4eDB\tau_i}\right)-\psi\left(\frac{1}{2}+\frac{\hbar}{4eDB\tau_e}\right)+\ln\left(\frac{\tau_i}{\tau_e}\right)\right] \quad (1.24)$$

Here $\psi$is the digamma function; τ_i and τ_e are the inelastic and elastic scattering times respectively; D is the diffusion constant. The elastic scattering time and the inelastic phase breaking time can be readily obtained from the magnetoconductivity measurement.

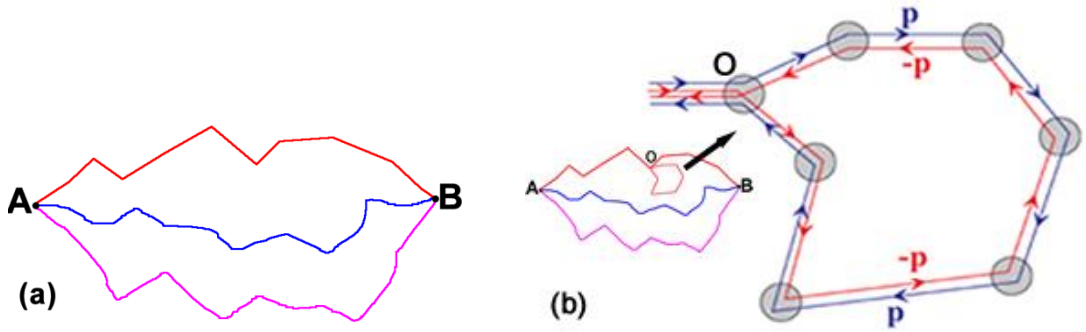

Figure 1.11 (a) Feynman's paths of a carrier propagating from A to B. The straight line between two scatterings represents the diffusive motion of carrier, just like a series of random walks. (b) A pair of closed paths at point O that contribute to weak localization.

For graphene, the weak localization is strongly modified due to valley degeneracy. Graphene lattice can be considered as a superposition of two identical sub-lattices with two atoms since atoms A and B are inequivalent. The two sublattices are like two degrees of freedom. The electron can have amplitude to be on the sublattice A, and an amplitude on sublattice B. The two components of the electronic wave function on them can be analogous to the two spins $\pm\frac{1}{2}$, called pseudo spin [30]. If all the electronic density is located on the A sublattice, this can be viewed as an "up" pseudo spin state, whereas density solely on the B sublattice corresponds to a "down" pseudo spin. In graphene, electronic density is usually shared equally between A and B sublattices, so that the pseudo spin part of the wave function is a linear combination of "up" and "down", and it lies in the plane of the graphene sheet [31,32], as shown in Fig. 1.12. Furthermore, quasiparticles in graphene are chiral [30], that means the orientation of the pseudo spin is

related to the direction of electronic momentum, either parallel or antiparallel to each other [31].

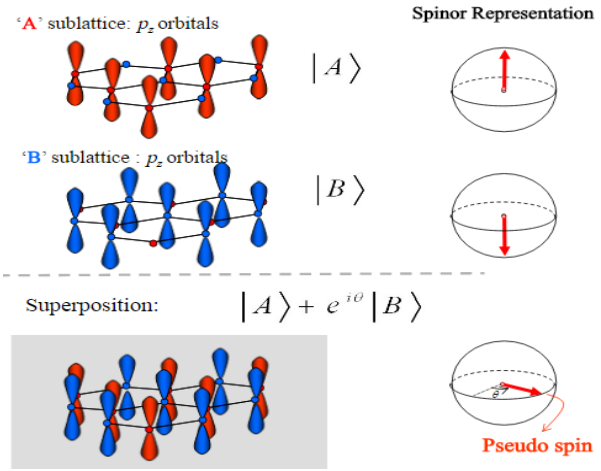

Figure 1.12 Pseudo spin of graphene [31].

When a carrier in graphene is scattered back to the origin after a series of scatterings, the momentum changes from $\vec{p} \rightarrow -\vec{p}$. Due to the chiral symmetry, the pseudo spin must also change to the opposite direction so that the pseudo spin remains parallel to the momentum. Hence for a clockwise path the pseudo spin rotates by an angle of $-\pi$, for a counterclockwise path the pseudo spin rotates by π. So the difference in the angle of pseudo spin rotation for the two paths is 2π. The net rotation of the pseudo spin by 2π induces a phase difference of π between the two paths [32,33]. This is analogous to the rotation by 2π of a spin–1/2 particle because a rotation by 2π doesn't return wave function to its origin state [34]. Hence the returning electron is out of phase, resulting in destructive interference. The probability to be scattered back to the origin is smaller due to the extra phase, and the conductivity is increased. This is called anti-localization.

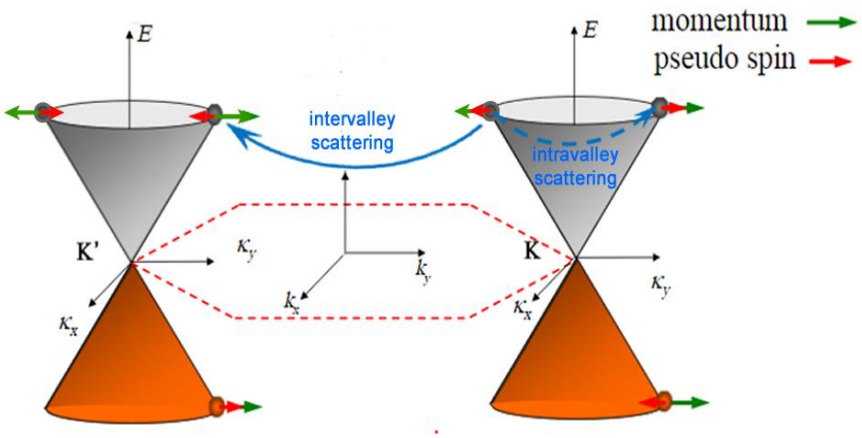

Figure 1.13 Chirality of graphene at Dirac points K and K'. Intravalley and intervalley scatterings play an important role in weak localization effect.

However, the trigonal warping effect [11,35] can break the time-reversal symmetry (the absence of $\vec{p} \rightarrow -\vec{p}$ symmetry) of the electronic dispersion within a single valley. Furthermore, elastic intravalley scattering can break the chiral symmetry. These two effects can suppress the weak antilocalization effect [36].

A carrier can be scattered from K to K', flipping the chirality. This is called intervalley scattering. In this process, the momentum has changed direction due to back scattering, but the psudospin has the same direction. So the phase acquired by two closed loops remains the same, resulting in the constructive interference and restoration of the conventional weak localization.

Hence due to the chiral nature of carriers in monolayer graphene, weak antilocalization is expected. However, trigonal warping and intravalley scattering suppresses antilocalization and intervalley scattering restores conventional weak localization. The change of magnetoconductivity, $\Delta\sigma(B) = \sigma(B) - \sigma(0)$, in graphene is [37-39]

$$\Delta\sigma(B) = \frac{e^2}{\pi h}\left[F\left(\frac{B}{B_\phi}\right) - F\left(\frac{B}{B_\phi+2B_i}\right) - 2F\left(\frac{B}{B_\phi+B_*}\right)\right. \quad (1.25)$$

$$F(z) = lnz + \psi(\frac{1}{2} + \frac{1}{z}),\ B_{\phi,i,*} = \frac{\hbar}{4De}\tau_{\phi,i,*}^{-1}$$

Here $\psi(z)$ is the digamma function, τ_ϕ is the inelastic phase breaking time, τ_i is the (elastic) intervalley scattering time, $\tau_*^{-1} = \tau_i^{-1} + \tau_w^{-1} + \tau_z^{-1}$, where τ_w is related to trigonal warping which breaks $\vec{p} \to -\vec{p}$ symmetry of the electronic dispersion and τ_z is the intravalley scattering time. D is the diffusion constant given by $D = {v_F}^2\tau/2$. τ is the transport scattering time obtained from the carrier mobility. Compared to the conventional 2EDG in Eq. (1.24), weak localization effect in graphene is more complex.

CHAPTER 2

DEVICE FABRICATION AND TRANSPORT MEASUREMENT

In this chapter, the fabrication of samples, including monolayer graphene with antidots and a Hall bar of AlInN/GaN heterostructure, is described in detail. The low temperature and high magnetic field techniques are also explained.

2.1 FABRICATION AND CHARACTERIZATION OF GRAPHENE WITH ANTIDOTS

Graphene sample is commercial monolayer graphene on Si/SiO_2 substrate (Graphene Supermarket Inc.), grown by the Chemical Vapor Deposition (CVD) method. The antidot lattice on graphene was fabricated by the electron beam lithography followed by reactive ion etching with oxygen plasma at the USC Nanocenter. A more detailed description can be found in Appendix A.

Figure 2.1 shows the Scanning Electron Microscope (SEM) images of the antidot lattice. The images are obtained by Zeiss Ultraplus Thermal Field Emission Scanning Electron Microscope. The grey region is graphene. However the white region is empty, where the graphene has been etched away by oxygen plasma. We can clearly see 4 Hall bars at up and down sides. The high magnification image of antidots, with the radius around r = 50 nm is displayed in Fig. 2.1(b).

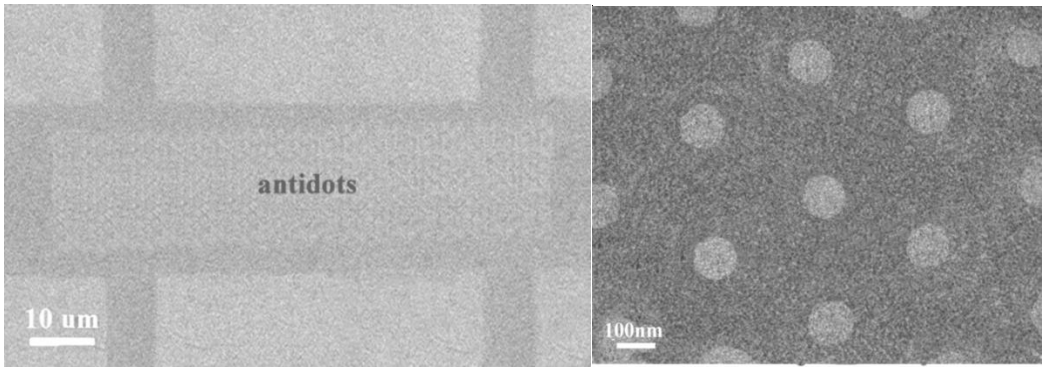

Figure 2.1 (a) Graphene antidots with Hall bars. (b) High magnification SEM image of antidots.

Raman spectroscopy (JY Horiba with a HeNe laser) of monolayer graphene is shown in Fig. 2.2. Clearly there are two prominent peaks. The band at ~2663 cm^{-1} is called the 2D peak which is due to the second order of zone-boundary phonons; the one at ~1602 cm^{-1} is G peak or Graphite peak [40]. The intensity ratio between 2D and G peak is an important indicator of the numbers of graphene layer. Monolayer graphene usually has a stronger 2D peak than a G peak. The intensity of the 2D peak decreases for a bilayer, triple layer and so on. The intensity high ratio between the 2D band and G band shows our graphene is monolayer.

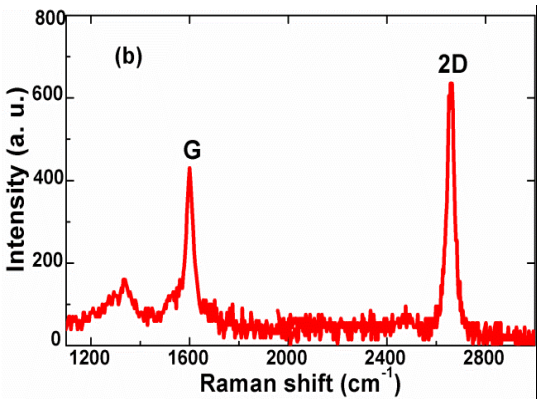

Figure 2.2 Raman spectroscopy of monolayer graphene.

2.2 FABRICATION OF ALINN/GAN DEVICE

The $Al_{0.83}In_{0.17}N$/GaN epilayer structures were grown on a sapphire substrate by standard metal-organic chemical vapor deposition (MOCVD) process. Our AlInN/GaN wafers were obtained from Dr. Asif Khan at the Electrical Engineering Department of USC. A SEM image of the cross section view of such heterostructure is provided in Fig. 2.3(a). It clearly shows a ~200 *nm* AlN buffer layer followed by ~2.2 *μm* undoped GaN as channel layer, ~1 *nm* AlN spacer and ~7 *nm* AlInN barrier layer with In composition of 17%.

In order to measure the transport properties, I fabricated a Hall bar using photolithography. The Hall bar mesa was etched by an inductive coupled plasma etching machine using Cl_2/BCl_3. A more detailed description is given in Appendix B. Fig.2.3(b) is a schematic diagram of our Hall bar.

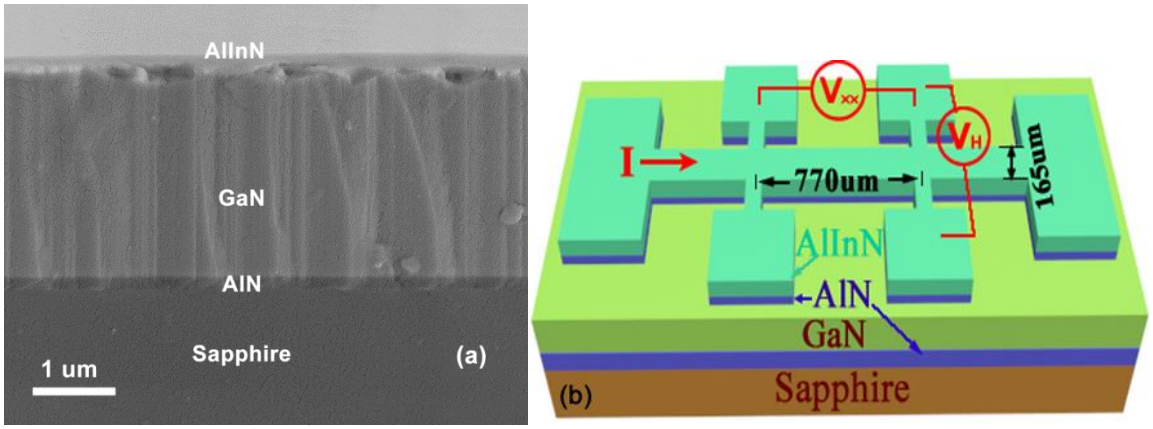

Figure 2.3 (a) SEM image of cross section of AlInN/GaN heterostructure. (b) Schematic diagram of a Hall bar.

2.3 THREE DIMENSIONAL CARBON NANOSTRUCTURES

Artificial opals are self-organized, close packed materials which are built up by nanoscale regular spheres. Figure 2.4 shows the structures of opal obtained by scanning electron microscope (Zeiss Ultra Plus FESEM). The opals are arranged in the hexagonal close-packed lattice. The diameter of the spheres is around 200 *nm*.

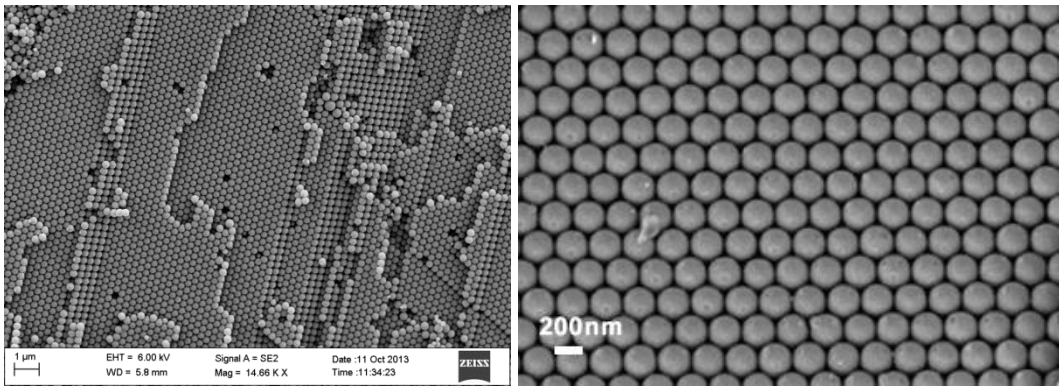

Figure 2.4 SEM images of artificial opal.

Our 3-dimensional carbon nanostructures were produced by infiltrating carbon into the porous matrix of artificial opals by chemical vapor deposition (CVD) of propylene gas and then removing the silica spheres with hydrofluoric acid [41]. The diameter of the spheres can be varied. The diameter of carbon inverse structure shown on the right of Fig. 2.5 is around 245 nm. We can also observe a mix of two structures, cubic and hexagonal.

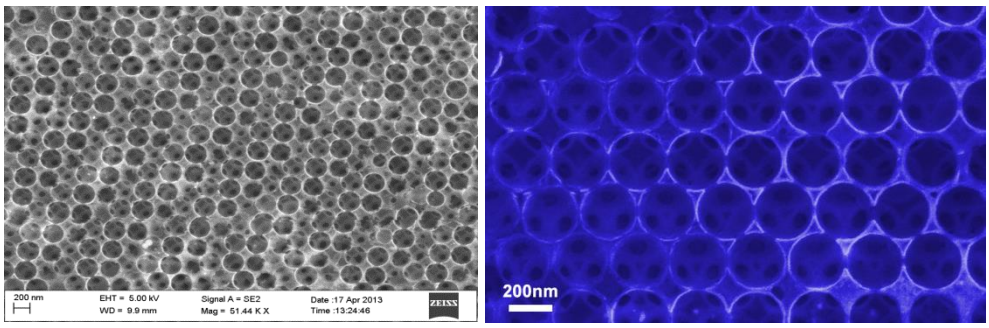

Figure 2.5 SEM images of 3-dimensional carbon nanostructure.

2.4 TRANSPORT MEASUREMENT TECHNIQUES

In our transport measurement, a 4- probe method is employed. The reason for using a 4-probe method instead of 2-probe is to reduce the contact resistance effect. In the 2-probe method shown in Fig. 2.6(a), a voltage source is applied to the sample and the current I is measured using Ampere meter. The current is determined not only by the sample resistance R_s, but also by the contact resistances R_{c1} and R_{c2}, which are all unknown. The measured current is smaller due to contact resistances. If we still use $R = \frac{V}{I}$ the resistance obtained is larger than the real sample resistance. However in the 4-probe method, a current source is applied, so the contact resistances R_{c1} and R_{c2} cannot affect the measured current I. When measuring the voltage on the sample, the contact resistances, R_{c3} and R_{c4}, are much smaller than the impedance of the volt meter. Thus the resistance obtained by $R = \frac{V}{I}$ is the real sample resistance.

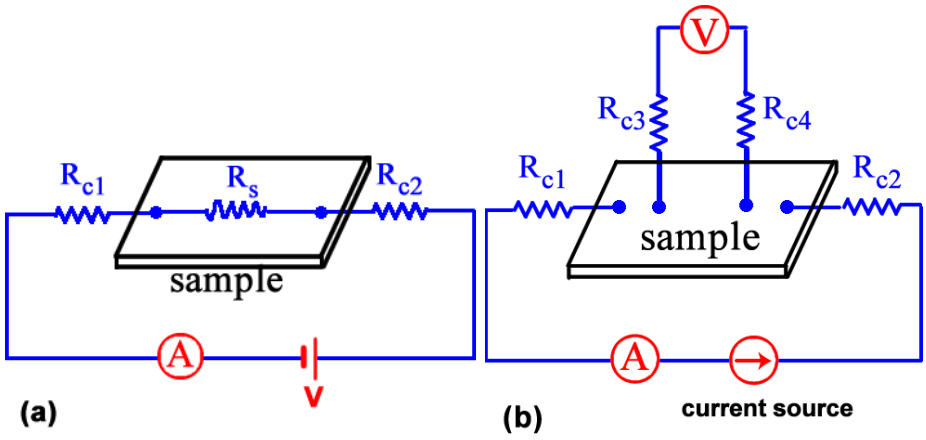

Figure 2.6 (a) 2-probe method, (b) 4-probe method.

Figure 2.7(a) shows the schematic diagram of probe connections for AlInN/GaN heterostructure. There are six pads in total. The largest two pads are connected to the

current source. The pair of probes on the same side are used to measure the longitudinal voltage V_{xx} and the two pads on opposite sides are for measuring the Hall voltage V_H. The magnetic field B is perpendicular to the sample surface, but we can also rotate the sample so that the orientation dependence of transport properties is obtained. Figure 2.7(b) shows a graphene sample with six gold pads connected to an 8-pin dip socket by aluminium wires. The size of the silicon substate is around 5 mm × 5 mm × 1 mm.

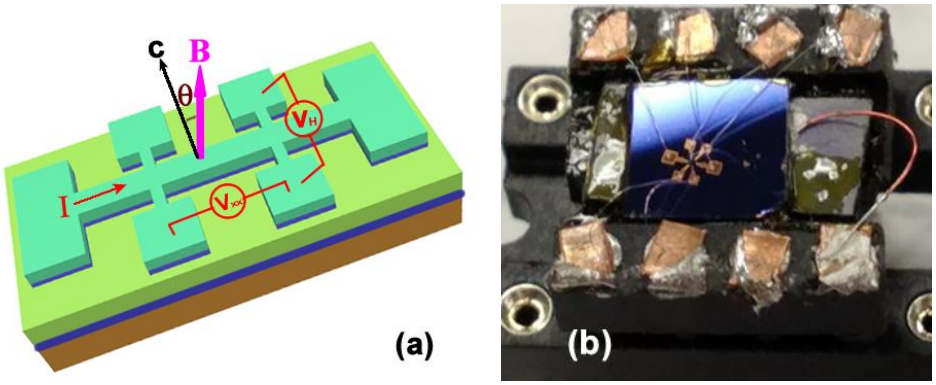

Figure 2.7 (a) schematic diagram of probe for the AlInN/GaN heterostructure. (b) Graphene sample on an 8-pin dip socket.

To reduce the noise and obtain a clean signal, we use lock-in amplifiers to measure the voltages. A 120 μA input current at 17.37 Hz was applied by the lock-in amplifier (Stanford SR850 DSP). The electrical and magneto transport measurements were conducted using an 18/20 Tesla General Purpose Superconducting Magnet (SCM2) and a 31 Tesla, 50 mm Bore Magnet (Cell 9) at the National High Magnetic Field Laboratory at Tallahassee, FL.

CHAPTER 3

QUANTUM TRANSPORT IN ALINN/GAN HETEROSTRUCTURES

The AlInN/GaN heterostructure is a wide band gap semiconductor that has great potential in high power and high frequency applications. In this chapter, I discuss my measurements of the transport properties of the two-dimensional electron gas in AlInN/GaN heterostructures at low temperatures. From the Shubnikov-de Haas oscillation and the change of the magnetoconductivity due to weak localization, I calculated the effective mass of the electrons and scattering times. The dominant scattering mechanisms at low temperatures have been determined.

3.1 TEMPERATURE DEPENDENT ELECTRICAL TRANSPORT

The typical temperature dependence of sheet resistance, $R_{\square}$ is shown in Fig. 3.1(a). Here sheet resistance is calculated by $R_{\square} = \frac{R_{xx}W}{L}$, where R_{xx} is the longitudinal resistance measured at zero-magnetic field; W=165 μm is the width of Hall bar; and L=770 μm is the length labeled in the figure. Generally the sheet resistance increases with increasing temperature above 20 K, consistent with metallic-like transport. The variation of the Hall carrier density as a function of temperature is shown in Fig. 3.1(b). The carrier density n is obtained by $R_H = \frac{B}{ne}$, where R_H is the Hall resistance, e is the charge of the electron and B is the magnetic field. Although the density increases with increasing temperature,

the change is very small. This is because the band gap is $E_g \sim 4$ eV [6,42], much larger than $k_B T$.

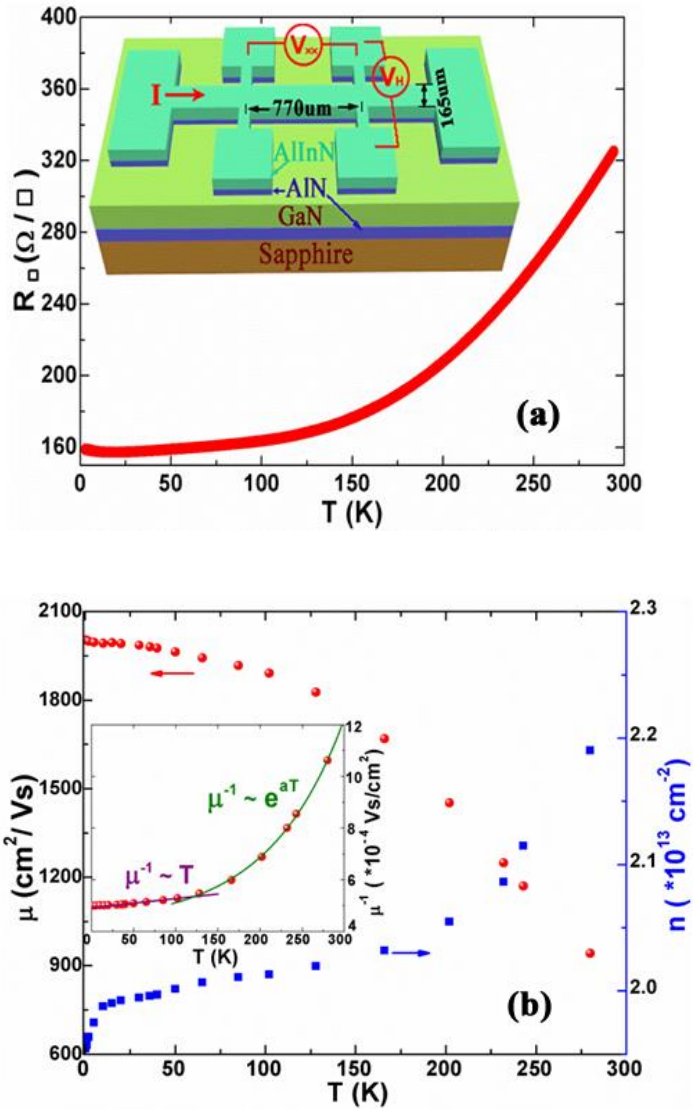

Figure 3.1 (a) Temperature dependent sheet resistance, inset is the schematic diagram of structure. (b) Carrier density and Hall mobility as a function of temperature.

In contrast, the Hall mobility decreases with increasing temperature, and the decreasing rate exhibits an interesting variation with temperature. Below 20 K, the

mobility is weakly temperature dependent. It decreases slightly with increasing temperature, mirroring that of the sheet resistance. As will be discussed later, these behaviors may arise from impurity scattering or surface roughness as well as electron-electron scattering. Between 20 K and 100 K, the temperature dependence is more pronounced. As shown in the inset of Fig. 3.1(b), the inverse mobility is directly proportional to temperature, $\mu^{-1} \propto T$, indicating that acoustic phonon scattering is dominant [43-45]. Such temperature dependence has been widely observed in AlGaN/GaN heterostructures. At higher temperatures, above 100 K, the mobility decreases even faster and an exponential dependence $\mu^{-1} \propto e^{aT}$ describes the data very well. In the 2DEG literature, such exponentially temperature dependent mobility at high temperatures has been attributed to polar optical phonon scattering [44,46].

3.2 SHUBNIKOV-DE HAAS OSCILLATION

The longitudinal resistance R_{xx} as a function of applied magnetic field B up to 18 T at different temperatures is shown in Fig. 3.2(a). As the magnetic field is increased, Shubnikov-de Haas (SdH) oscillations appear. The peaks of the oscillations are pronounced at low temperatures and damped with increasing temperature. This effect of temperature is more apparent if we subtract the background from R_{xx}, (Fig. 3.2(b)). SdH oscillations are a periodic function of *1/B*. Evidence of multiple subbands in AlInN/GaN or AlGaN/GaN heterostructures has been reported [28,47]. However, Fourier Transform analysis of our data for ΔR_{xx} results in a single peak frequency B_F = 403 T as shown in the

inset of Fig. 3.2(b). This indicates that only one band is dominant in our sample. Also the frequency B_F is directly related to the carrier density by

$$n_{SdH} = 2eB_F/h \tag{3.1}$$

The factor of two is due to spin degeneracy. Hence the carrier density of this sample is $n_{SdH} = 1.948 \times 10^{13} cm^{-2}$. This agrees very well with the average value obtained from our Hall measurement.

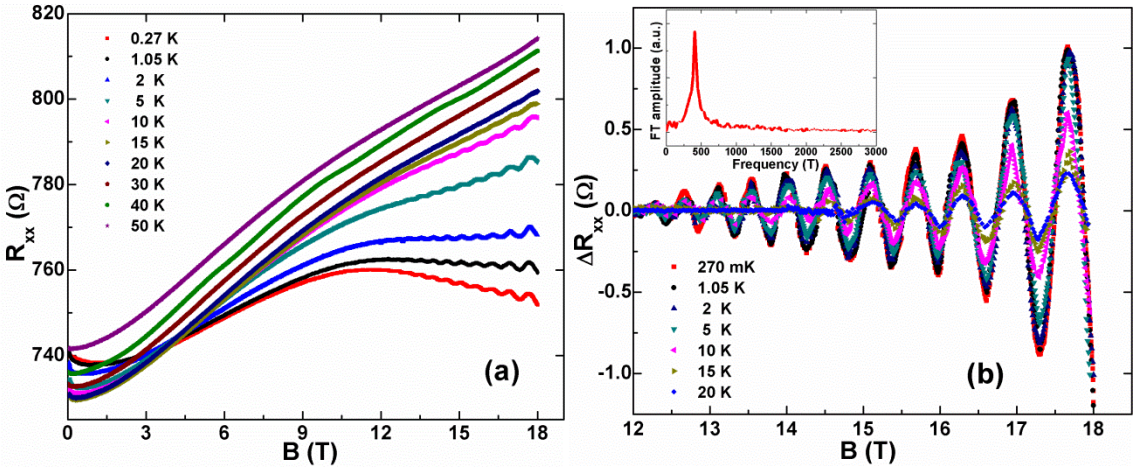

Figure 3.2 (a) Magnetoresistance up to 18 T at a set of temperatures. (b) Shubnikov-de Haas oscillations after subtracting the background.

The amplitude of the SdH oscillation is given by [48,49]

$$\Delta R_{xx} = 4R_0 \frac{\chi}{\sinh(\chi)} \exp\left(\frac{-\pi}{\omega_c \tau_q}\right) \tag{3.2}$$

Here τ_q is the quantum lifetime, which will be discussed later. $\chi = 2\pi^2 k_B T/\Delta E$ and the Landau level energy gap is $\Delta E = \hbar\omega_c = \hbar eB/m^*$.

The effective mass $m^*$of electrons can be extracted from the temperature dependence of the SdH amplitude at a constant magnetic field by examing the following ratio [9]

$$\frac{\Delta R_{xx}(T,B)}{\Delta R_{xx}(T_0,B)} = \frac{T sinh(\chi(T_0))}{T_0 \sinh(\chi(T))} = \frac{T \sinh(2\pi^2 k_B T_0/\Delta E(B))}{T_0 \sinh(2\pi^2 k_B T/\Delta E(B))} \quad (3.3)$$

Here we chose the lowest temperature, 0.27 K, as T_0. Figure 3(a) shows the above ratio of amplitude at T_0 = 0.27 K and B = 17.7 T. Analyzing our data using Eq. (3.3) we can extract $\Delta E(B)$. The inset of Fig. 3.3(a) shows the field dependence of Landau level energy gap. Thus the corresponding effective mass is $m^* = (0.2327 \pm 0.0019)m_e$, similar to the values reported in AlInN/GaN heterostructures which are $0.22\,m_e$ and $0.25m_e$ [47,50] and in AlGaN/GaN systems which are $0.23m_e$ and $0.24m_e$ respectively [5,51].

The quantum lifetime is obtained from the slope of the Dingle plot, as shown in Fig. 3.3(b), because

$$ln\mathfrak{D} = \ln[\frac{\Delta R(T,B)\sinh(2\pi^2 k_B T/\Delta E(B))}{2\pi^2 k_B T/\Delta E(B)}] = C_0 - \frac{\pi m^*}{e\tau_q B} \quad (3.4)$$

where $\mathfrak{D}$ is the expression within the bracket, C_0 is a constant. In this sample the quantum lifetime is $\tau_q = 0.0350 \pm 0.0017\,ps$. Furthermore, τ_q also determines the Dingle temperature $T_D = h/(4\pi^2 k_B \tau_q)$, which is a measure of the disorder. At T = 0.27 K, we find a relatively high value $T_D = 34.7$ K. Also the broadening of the Landau levels [48,49], as determined by $k_B T_D$ ~3 *meV*, is not much smaller than the Landau level spacing $\Delta E(B) = 9.04\,meV$ at 17.7 T. This may explain the relatively small amplitude ($\Delta R_{xx}/R_{xx} \ll 1$) of the SdH oscillations.

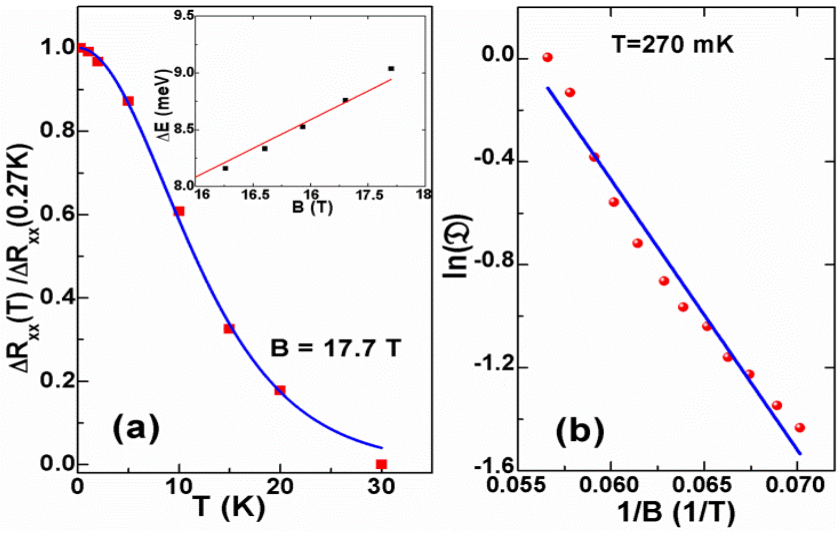

Figure 3.3 (a) Effective mass plot at 17.7 T, where the data are best fit to Eq. (3.3); Inset is field dependence of the Landau level spacing. (b) Dingle plot to obtain the quantum lifetime in AlInN/GaN heterostructure.

It is instructive to compare the quantum relaxation rate to transport rate, since

$$1/\tau_q = \int P(\theta) d\theta$$

$$1/\tau_t = \int P(\theta)(1 - cos\theta) d\theta \qquad (3.5)$$

where $P(\theta)$ is the probability of scattering through an angle θ. The quantum lifetime τ_q includes information of all scatterings; however the transport lifetime τ_t (from Hall mobility) is weighted by the scattering angle and mainly determined by large angle scattering [51-53]. The transport lifetime $\tau_t = 0.252\ ps$ is nearly an order of magnitude larger than the quantum lifetime. In particular the ratio $\tau_t/\tau_q = 7.2$ indicates that small angle scattering associated with long range interactions due to distant ionized impurities is the dominant scattering mechanism in our sample.

3.3 WEAK LOCALIZATION

As is evident from Fig. 3.2(a), at low magnetic fields R_{xx} decreases with the applied field; that is conductivity goes up with increasing field. This negative magnetoresistance arises from weak localization. It is convenient to define the magnetoconductivity by $\sigma_{xx} = \rho_{xx}/(\rho_{xx}^2 + \rho_{xy}^2)$. The quantum correction to the change in magnetoconductivity at low magnetic fields is [5,28,29,54]

$$\Delta\sigma_{xx} = \sigma_{xx}(B) - \sigma_{xx}(0) = \frac{e^2}{\pi h}\left[\psi\left(\frac{1}{2} + \frac{\hbar}{4eDB\tau_i}\right) - \psi\left(\frac{1}{2} + \frac{\hbar}{4eDB\tau_e}\right) + \ln\left(\frac{\tau_i}{\tau_e}\right)\right] \qquad (3.6)$$

Here ψ is the digamma function; τ_i and τ_e are the inelastic and elastic scattering times respectively; D is the diffusion constant given by $D = {v_F}^2\tau/d = {v_F}^2\tau/2$, where d is the dimensionality and for our two-dimensional (d = 2) system the Fermi velocity is

$$v_F = \hbar k_F/m^* = \hbar\sqrt{2\pi n}/m^* \qquad (3.7)$$

Here $v_F = 0.5504 \times 10^6 m/s$. By choosing parameter values estimated earlier $\tau \equiv \tau_t = 0.252\ ps$, we determined $D = 0.03817 m^2/s$ and the mean free path $l = v_F\tau_t = 139\ nm$ [10].

The inelastic and elastic scattering times were computed from the best fit analysis of experimental data to Eq. (3.6). $\Delta\sigma_{xx}$ for a set of temperatures is shown in Fig. 3.4(a). For a constant temperature the conductivity increases with increasing magnetic field, and at higher temperature, the conductivity is reduced. We find that Eq. (3.6) describes the experimental data very well for temperatures below 20 K, which allows us to obtain the values of the relaxation times. Interestingly the elastic scattering time τ_e is constant with temperature; this may be due to the short range interactions such as impurity or interface

roughness scatterings. Also $\tau_e = 0.144ps$ is the same order as the transport time τ_t. However, the inelastic scattering time τ_{in} is much larger than the elastic scattering time and the transport time at low temperatures. This is necessary because the phase coherence length should be long enough so that the carrier can be scattered back to the origin after several scatterings. In addition τ_{in} decreases with increasing temperature. In fact, the inelastic scattering rate is linearly proportional to temperature, ${\tau_{in}}^{-1} \propto T$, as shown in Fig. 3.4(b). This linearity has been attributed to phase breaking by inelastic electron-electron scattering [28,55,56].

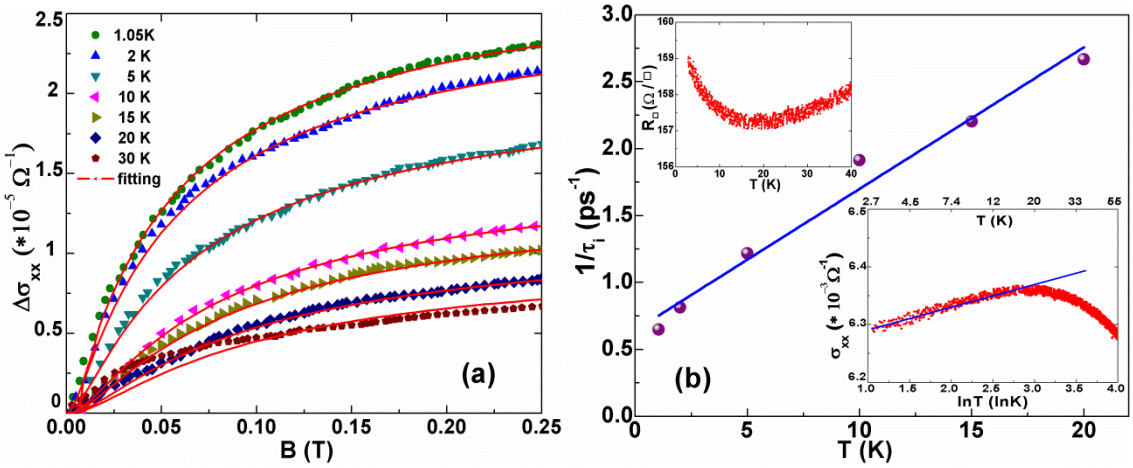

Figure 3.4 (a) Magnetoconductivity at low magnetic fields for several temperatures. (b) The inelastic scattering rate displays linear temperature dependence. Insets are the zero-field resistance and conductivity respectively.

The effect of electron-electron scattering is also observed in the absence of the magnetic field. As shown in the inset of Fig. 3.4(b), the sheet resistance at low temperatures is non-monotonic. With increasing temperature it first decreases until 20 K and then increases. This enhanced conductivity for less than 20 K is also due to weak localization. The quantum interference correction at zero magnetic field is [29,57],

$$\sigma_{xx}(B=0) = \lim_{B\to 0} \frac{e^2}{\pi h}\left[\psi\left(\frac{1}{2}+\frac{\hbar}{4eDB\tau_{in}}\right) - \psi\left(\frac{1}{2}+\frac{\hbar}{4eDB\tau_e}\right)\right] \cong -\frac{e^2}{\pi h} ln\frac{\tau_{in}}{\tau_e} \qquad (3.8)$$

since $\psi(x) \to lnx\ when\ x \gg 1$.

As stated above, $\tau_{in} \propto T^{-1}$, thus $\sigma_{xx}(0) \propto lnT$ [58]. The conductivity at zero-field is plotted as a function of *lnT* in the inset of Fig. 3.4(b). Clearly below 20 K, $\sigma_{xx}(B=0)$ displays a linear dependence, characteristic of weak localization. Hence at low temperatures, we observed the experimental evidence of weak localization in zero-field transport as well as the magnetotransport in our AlInN/GaN system, both hallmarks of electron-electron scattering.

3.4 ANGLE DEPENDENCE

To further investigate weak localization behavior, we varied the angle θ between magnetic field and the normal to the surface of sample. Figure 3.5 shows the angle-dependent resistance at T = 2 K. At 0°, when magnetic field is perpendicular to the sample, the magnetoresistance is pronounced and similar to the behavior described earlier. With the increase of tilt angle, the influence of the magnetic field becomes smaller and weak localization is maintained over higher magnetic fields. At the highest tilt angle (θ = 88°), effects of weak localization dominate the entire field regime such that the resistance continues to decrease with increasing magnetic field, displaying a negative magnetoresistance even up to 18 T. The crossover field where the magnetoresistance is lowest displays the anticipated linear dependence on 1/*cosθ*. Furthermore, the SdH oscillations disappear gradually with increasing angle. If we plot the magnetoresistance as a function of the perpendicular component of the magnetic field, *Bcosθ*, the peaks

collapse respectively for different angles, as shown in Fig. 3.5(b). Therefore, the behavior is controlled only by the perpendicular magnetic field, confirming the two dimensional nature of electron transport in this heterostructure [9,10,49].

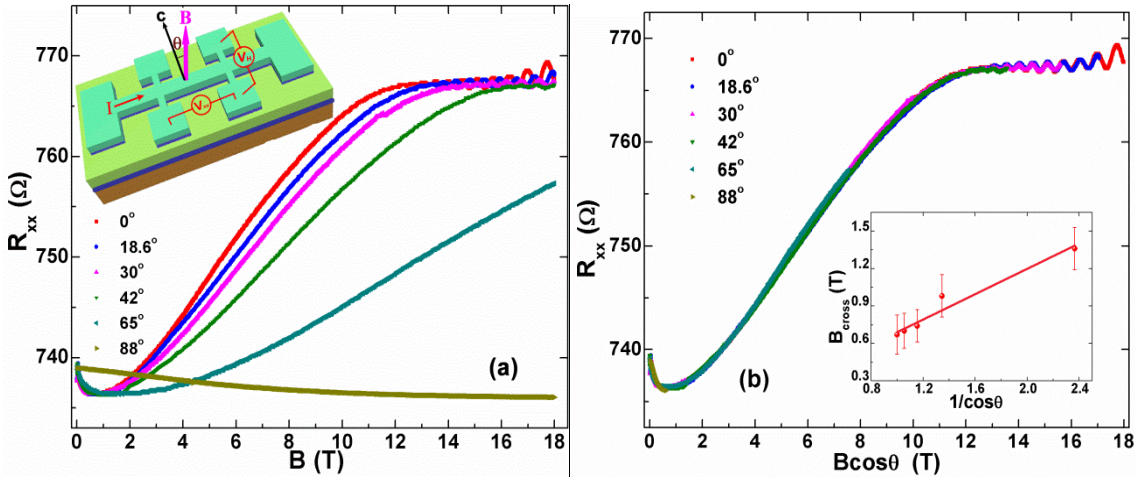

Figure 3.5 (a) Angle dependence of the magnetoresistance at 2 K. (b) The magnetoresistance as a function of the perpendicular field, all data collapse to a single curve.

3.5 COMPARISON WITH OTHER SAMPLES

The sample discussed earlier, labeled as sample A, shows small amplitude Shubnikov-de Haas oscillations. In comparison, sample B, deposited under different conditions with slightly lower carrier density $n_{SdH} = 1.53 \times 10^{13} cm^{-2}$, has a larger amplitude SdH oscillation. As shown in Fig. 3.6(a), the maximum of ΔR_{xx} for sample B is around 10 Ω, one order of magnitude bigger than that of sample A. In specimen B the quantum lifetime is $\tau_q = 0.074\, ps$, which is also smaller than the transport lifetime. The ratio $\tau_t/\tau_q = 6.1$, although slightly less than the ratio in sample A, still indicates that small angle scattering is the dominant scattering mechanism. Moreover, the change of conductivity $\Delta\sigma$ due to weak localization in sample B is larger than that in sample A (Fig. 3.6(b)). Hence the

interference is much stronger. The analysis of Eq. (3.6) shows that the inelastic scattering time of sample B is correspondingly bigger than that of sample A.

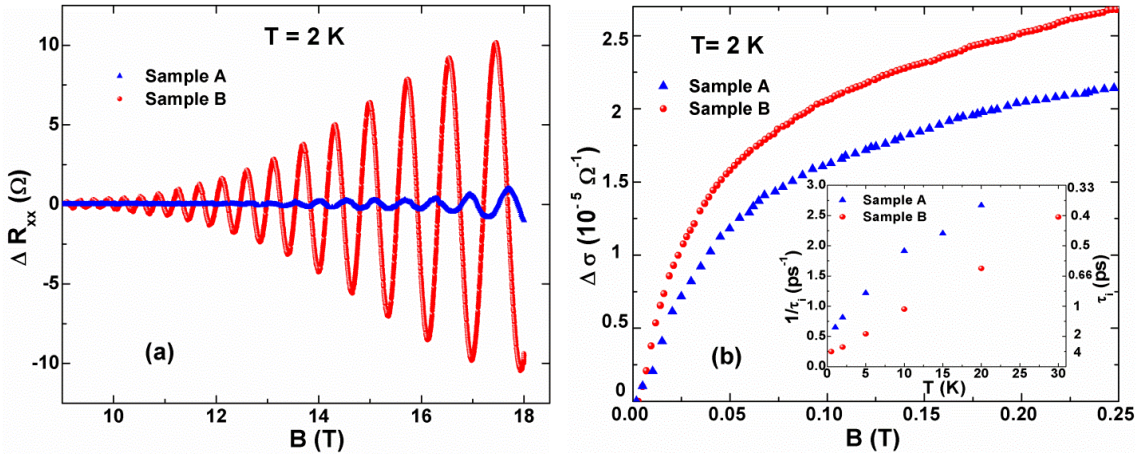

Figure 3.6 (a) Shubnikov-de Haas oscillations for two samples. Clearly, Sample B has stronger SdH oscillations. (b) weak localization of two samples at 2 K. Inset is the inelastic relaxiation time as a function of temperature.

Table 3.1 lists the carrier density, the quantum (τ_q), transport (τ_t) lifetimes and inelastic scattering time (τ_i) in related systems. Qualitatively, the inelastic scattering rate should be smaller than transport rate, which in turn is less than the quantum relaxation rate ($\frac{1}{\tau_i} < \frac{1}{\tau_t} < \frac{1}{\tau_q}$). Indeed, for both samples A and B, τ_q is the shortest, and about an order of magnitude smaller than τ_t, as expected when small angle scattering is dominant. Furthermore, the inelastic time scale is the longest, and much longer than quantum and transport lifetimes. This same trend in time scales is also reported in other AlGaN/GaN systems, as can be seen in table 3.1.

Physically, the SdH effect arises from the tuning of density of states as well as the Fermi level by the magnetic field. With increasing magnetic field, Landau levels

periodically cross the Fermi level, resulting in oscillations of conductance. Whereas, weak localization is associated to non-classical back scattering of the carrier to the origin, where small angle scattering by long range interaction is ineffective for this process [27]. As a matter of fact, weak localization is an interference phenomenon hence sensitive to the phase of the wavefunction. At low temperatures, although small-angle scattering is frequent, only interactions that destroy phase coherence such as electron-electron and electron-phonon scatterings play important roles in the weak localization process [59]**.**

Table 3.1 Comparison of Shubnikov-de Haas oscillation and weak localization parameters in GaN based 2DEG. The inelastic scattering time is the value at the lowest temperature respectively.

System	Carrier density ($10^{13}\mathrm{cm}^{-2}$)	Quantum lifetime $\tau_q(ps)$	Transport lifetime $\tau_t(ps)$	Inelastic time $\tau_i(ps)$
$Al_{0.83}In_{0.17}N/GaN$ (A)	1.94	0.035	0.252	1.66
$Al_{0.83}In_{0.17}N/GaN$ (B)	1.53	0.074	0.45	4.02
$Al_{0.25}Ga_{0.75}N/GaN$(ref.[5])	1.01	0.050	0.26	4.00
$Al_{0.22}Ga_{0.78}N/GaN$(ref.[60])	1.25	0.078	0.13	4.67

In conclusion, weak localization is observed for the first time in AlInN/GaN heterostructures at low temperatures (T < 20 K). The zero-field conductivity varies as *lnT* and the magnetoconductivity increases with increasing magnetic field for low fields, both of which are hallmarks of weak localization. We find electron-electron scattering is the dominant phase breaking mechanism in this temperature range. At high magnetic fields, the resistance below 20 K exhibits Shubnikov-de Haas oscillations. The large ratio between the transport and quantum lifetimes indicates small angle scattering is dominant at low temperatures. Our angle dependent measurement shows that the magnetoresistance

scales with $B\cos\theta$, confirming the two dimensionality of system. Below 20 K the carrier mobility is weakly reduced with increasing temperature. In contrast, above 20 K the mobility rapidly decreases with increasing temperature as the source of scattering changes from acoustic phonons to optical phonons.

Electron-electron scattering, small angle scattering due to long-range Coulomb interactions, acoustic phonons and optical phonons all progressively contribute to the decrease in mobility with rising temperature for the 2DEG in AlInN/GaN heterostructure.

CHAPTER 4

QUANTUM TRANSPORT AND BAND GAP OPENING IN MONOLAYER GRAPHENE WITH ANTIDOTS

Due to the unique band structure, graphene has remarkable properties such as ultra high mobility, massless Dirac fermions and long mean free path. It is expected to be a promising candidate for next generation electronic devices. However graphene has no bandgap [3,61]. In order to open a band gap for applications, several strategies have been proposed including graphene nanoribbon [12,13], antidot lattice [14], heterostructure and chemical doping.

An antidot lattice is a regular array of holes. Antidot arrays impose lateral potential barriers that create a bandgap in graphene. The size of the gap can be tuned by adjusting the antidot lattice parameters. As reported in theoretical studies, the gap can be as large as 1 eV with the size of antidot as small as 10 *nm* [14,62-64]. However, there are few experimential studies about band gap in antidot graphene [15].

Graphene antidot lattices display many interesting transport properties especially in magnetic fields where the competing length scales lead to rich physics. Many quantum effects such as Shubnikov-de Haas oscillations, weak localization, commensurability oscillations and the spin-orbit interaction have been observed [65]. It has becom a great ground on which to investigate such fundemantal physics.

In this chapter, we studied quantum transport of chemical vapor deposited (CVD) monolayer graphene on a SiO_2/Si substrate with hexagonal arrays of antidots. We observed weak localization and prominent Shubnikov-de Haas (SdH) oscillations. From the temperature dependent amplitude of the SdH oscillation and the Dingle plot, the effective mass of the electron and the quantum scattering time are obtained. We demonstrate that the radius of the antidots greatly affects the properties of graphene. With increasing radius, the carrier density is decreased and effective mass is also reduced. Furthermore, a band gap ~ 10 *meV* is opened due to the introduction of antidots lattice.

4.1 SHUBNIKOV DE-HAAS OSCILLATION

Fig. 4.1(a) shows scanning electron microscope (Zeiss Ultra Plus FESEM) images of one sample. The antidot lattice is simiply a triangular array of holes. The radius of the antidot and lattice constant can be varied. For simplicity, the distance between nearest antidot edge is 200 *nm* and fixed. The radius of antidot is varied and here we compare r = 125 *nm*, r = 50 *nm* (Fig. 4.1 (a)) and r = 0 *nm* (CVD graphene).

Electrical and magneto transport measurements were conducted in a 31-Tesla magnetic field, 50 mm Bore Magnet (cell 9) with ^{3}He insert at the NHMFL. The magnetoresistance at a set of temperatures for graphene antidots with radius r = 50 *nm* is shown in Fig. 4.1(b).

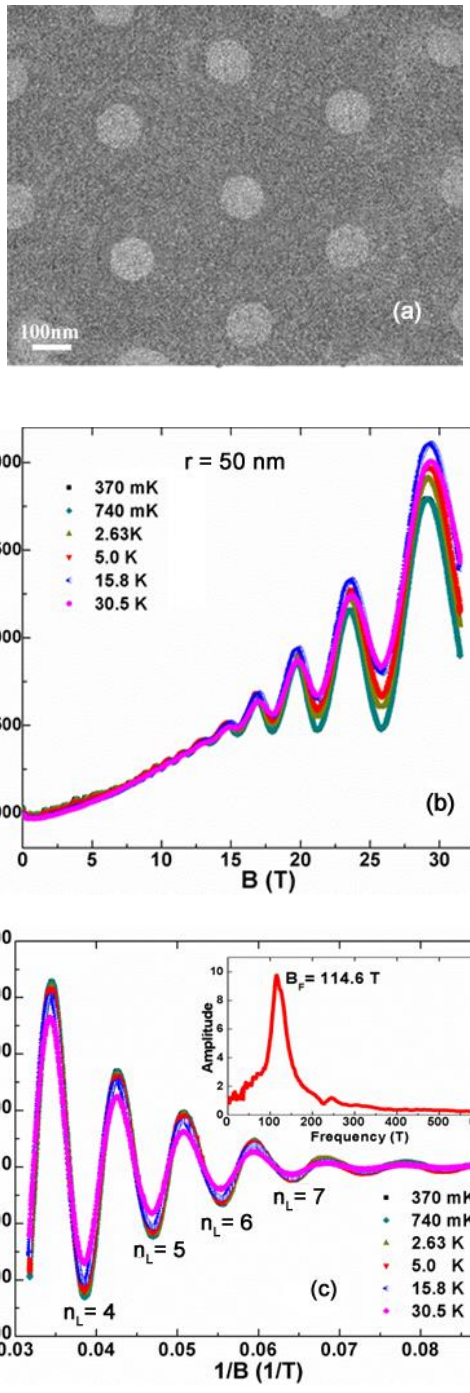

Figure 4.1 (a) SEM image of graphene with antidots. The radius of antidot is around 50 *nm*. (b) Magnetoresistance as a function of magnetic field for a set of temperatures for monolayer graphene with *r* =50 *nm* antidots. (c) Shubinikov de-Haas oscillations as a function of 1/B after subtracting the background. Fourier transform analysis is shown in the inset.

With increasing magnetic field, R_{xx} first becomes smaller, showing negative magentoresistance due to the suppression of weak localization. This will be discussed later. Above 7 T, Shubnikov de-Haas oscillations appear and become prominent at larger fields. In order to see the oscillations clearly, the background has been removed and ΔR_{xx} is shown as a function of 1/B in Fig. 4.1(c). Here the background is determined by averaging the curves connecting the maxima and minima respectively. Clearly these oscillations exhibit temperature dependence. The amplitude becomes smaller with increasing temperature.

The SdH oscillation can be expressed by [2,66]

$$\Delta R_{xx} = R_0 \frac{\chi}{\sinh(\chi)} \exp\left(\frac{-\pi}{\omega_c \tau_q}\right) \cos[2\pi\left(\frac{B_F}{B} + \frac{1}{2} + \beta\right)] \tag{4.1}$$

where $\chi = 2\pi^2 k_B T/\Delta E$, $\Delta E = \hbar\omega_c = \hbar eB/m^*$. k_B is the Boltzmann constant, $\hbar$ is the reduced Planck constant, e is the electron charge, τ_q is the quantum lifetime, β is the associated Berry phase and B_F is the oscillation frequency in Tesla, which is the magnetic field of the n=0 Landau level. The SdH oscillation is periodic in *1/B* and Fourier transform analysis shows the frequency is B_F = 114.6 T as shown in the inset of Fig. 4.1(c). Since

$$n_{SdH} = 4eB_F/h = 2eB_F/(\pi\hbar) \tag{4.2}$$

Here the factor of four is due to four-fold degeneracy of the spin and valley in graphene, in contrast to 2DEG in AlInN/GaN heterostructure where $n_{SdH} = eB_F/(\pi\hbar)$. The carrier density of r = 50 *nm* graphene antidots is $n_{SdH} = 1.108 \times 10^{13} cm^{-2}$.

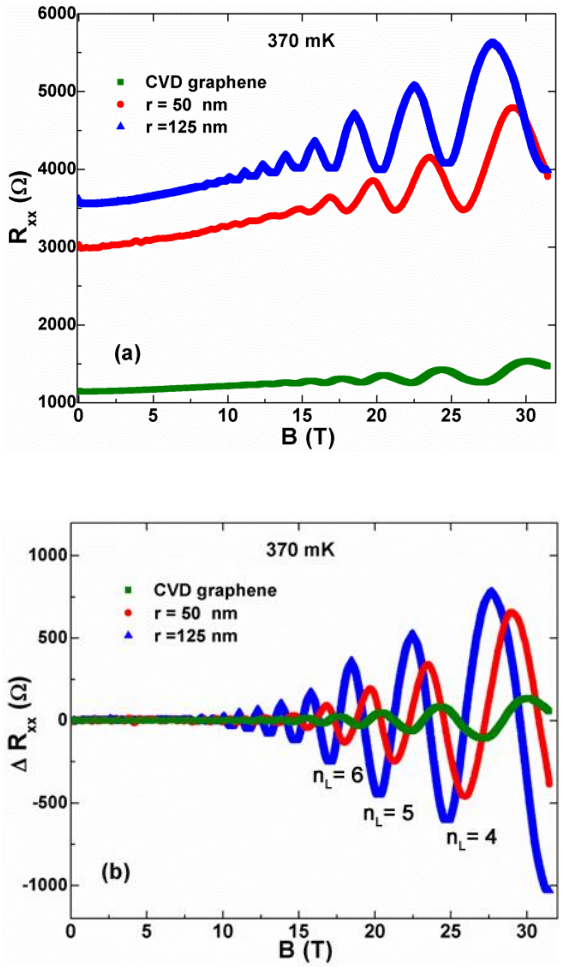

Figure 4.2 (a) Magnetotransport for monolayer graphene with different radii antidots and pure graphene at 370 mK. (b) SdH oscillations after subtracting the background.

In order to know the effect of the antidot array, monolayer graphene with different antidot radii have been fabricated and measured as shown in Fig. 4.2(a). Three effects can be seen. First, the introduction of antidots increases the resistance of sample. Graphene without antidots has a much smaller resistance than samples with antidots. Second, the magnitude of oscillations is enhanced by the antidots. With increasing magnetic field, SdH oscillations appear for all the samples, but when the antidot array is introduced and the radius increased, the oscillation becomes prominent as in Fig. 4.2(b). The peak value

is almost 800 Ω for r = 125 *nm* at 28 T, whereas it is only 140 Ω at 30 T for CVD graphene without antidots (r = 0 *nm*). Furthermore, the maxima move to lower magnetic fields with increasing antidot size. For the same Landau level, for example n_L = 4, the magnetic field is 27.2 T, 25.9 T, and 24.7 T for r = 0 *nm*, 50 *nm*, and 125 *nm* antidot samples rescpectively. Hence the antidot size indeed affects the properties of graphene.

The Landau fan diagram [1,67] is shown in Fig. 4.3(a). The intercept with the N axis is the associated Berry phase β. From the fitting, $\beta \sim 0.39 \pm 0.04$, 0.67 ± 0.06, 0.53 ± 0.02 for r = 0, 50, and 125 *nm* graphene antidot samples respectively. The value for r = 125 *nm* antidots is very close to 0.5, corresponding to the Berry phase $\varphi_B = 2\pi\beta \cong \pi$, indicating the presence of Dirac fermions. But the values for CVD graphene and 50 *nm* antidots are a little off from 0.5. Furthermore, the slope of the linear fit for each sample is different. CVD graphene has the largest slope. With increasing antidot radius the slope which is proportional to B_F becomes smaller; therefore the SdH oscillation frequency B_F becomes smaller. By $n_{SdH} = 2eB_F/(\pi\hbar)$, the carrier density of CVD graphene is largest and it is reduced with the increase in antidot size. The reason for this can be understood as follows. Since the nearest edge to edge distance is fixed, the number of antidots becomes less when the radius of antidots is increased. In the constant area, the total area of antidots is still increased in our sample. So the area with graphene is decreased, the total number of carriers is also decreased. In addition, the carrier density is affected by the interplay between the graphene and the substrate, especially by charged impurities [68]. The reduction of contact area between the graphene and the substrate leads to less carriers transferred to the graphene [69]. The suspended graphene usually has a smaller

carrier density [70]. Hence the carrier density is decreased with increasing antidot size in our graphene samples.

The effective mass m^*can be extracted from the temperature dependence of the SdH amplitude at a constant magnetic field by [71]

$$\frac{\Delta R(T,B)}{\Delta R(T_0,B)} = \frac{T \sinh(2\pi^2 k_B T_0/\Delta E(B))}{T_0 \sinh(2\pi^2 k_B T/\Delta E(B))} \tag{4.3}$$

Here we chose the lowest temperature 0.37 K as T_0. The Landau level spacing values $\Delta E(B) = \hbar eB/m^*$ for different magnetic fields are obtained from the best fit using Equation (4.3) and are shown in Fig. 4.3(b). Hence the effective mass $m^*$is obtained from the slope of the linear fit. For all three samples, CVD graphene has the smallest slope. And with increasing antidot radius the slope increases. The effective masses are $(0.0875 \pm 0.0047)m_e$, $(0.0775 \pm 0.0023)m_e$, $(0.064 \pm 0.0021)m_e$ respectively for CVD graphene, *r* = 50 *nm* and *r* = 125 *nm* antidot samples, shown in Table 4.1. All the effective masses are very small, implying the nature of massless Dirac particles. Clearly, the introduction of an antidot lattice has impact on the effective mass of the electrons. It is interesting that m^* becomes smaller with increasing antidot radius. Generally antidots should introduce more scattering than that in the CVD graphene, which suppresses the motion of electrons, resulting in a larger effective mass. But our experimental observation is opposite. The reason is [11]

$$m^* = \frac{E_F}{v_F^2} = \frac{\hbar k_F}{v_F} = \frac{\hbar\sqrt{\pi}}{v_F}\sqrt{n} \tag{4.4}$$

here $k_F^2/\pi = n$ and $E_F = \hbar v_F k_F$ [11,23]. The effective mass depends on the square root of electron density *n*, which has been widely observed in graphene [1,66,72]. Since the

CVD graphene without antidots has a larger carrier density, the effective mass is consequently larger.

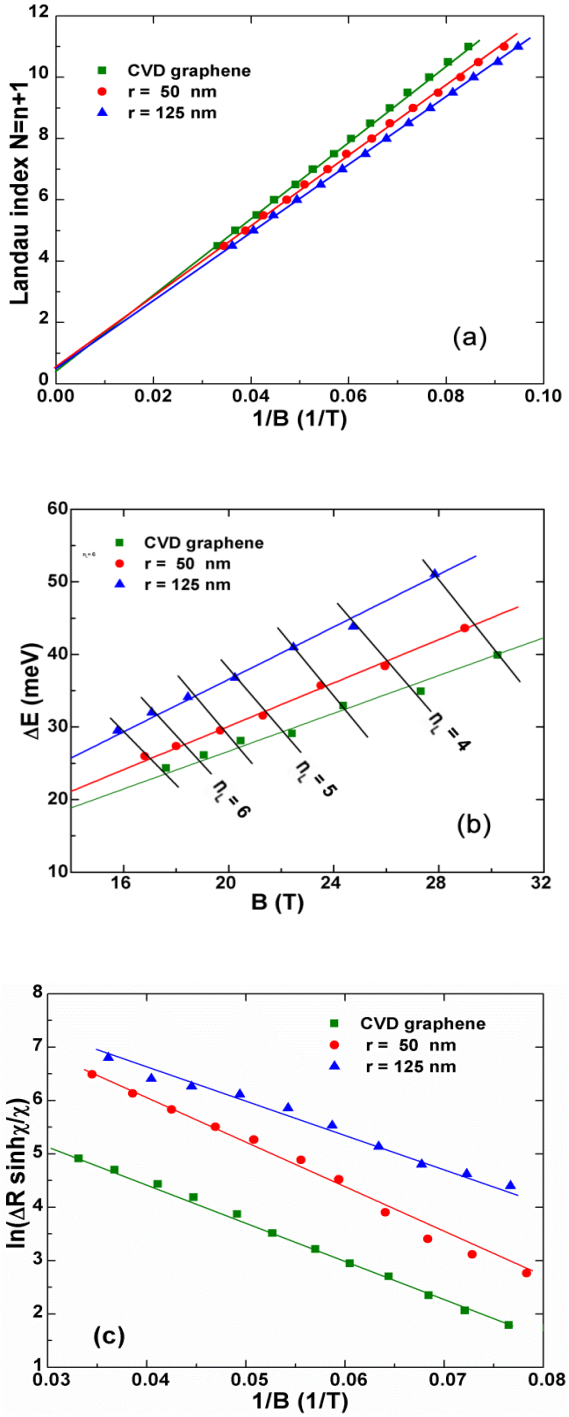

Figure 4.3 (a) Landau fan diagram. (b) Field dependence of Landau level spacing. (c) Dingle plot to obtain the quantum lifetimes at T= 0.37 K.

The quantum lifetime is obtained from the Dingle plot [71]

$$ln\,[\Delta R(T,B)\sinh(\chi)/\chi] \propto -\pi m^*/(e\tau_q B) \tag{4.5}$$

Figure 4.3(c) shows the data at T = 0.37 K. The quantum lifetime from this Dingle equation is $\tau_q = 0.016\,ps$ for r = 50 nm antidot graphene. This corresponds to a Dingle temperature $T_D = \hbar/(2\pi k_B \tau_q) = 74\,K$; the broadening of the Landau levels, obtained by $k_B T_D$ ~6.4 meV, is much smaller than Landau level spacing $\Delta E(B) = 43.6\,meV$ at 29 T. This explains the prominent amplitude of the oscillations. Furthermore, the quantum lifetime is smaller than the transport lifetime obtained from Hall mobility $\tau_t = 0.024$ ps. Quantum lifetime includes contributions from all scattering mechanisms; however the transport lifetime is mainly determined by large angle scattering. The ratio $\tau_t/\tau_q = 1.5$, indicating small-angle scattering associated with long range Coulomb interaction is of significance [38,55,73].

Table 4.1 Electronic and transport parameters for graphene antidot samples.

Antidot Radius (nm)	Carrier density ($10^{13} cm^{-2}$)	Effective mass m^*	Quantum lifetime $\tau_q(ps)$
r = 0	1.225	0.0875 m_e	0.022
r = 50	1.108	0.0775 m_e	0.016
r =125	1.067	0.0640 m_e	0.018

4.2 WEAK LOCALIZATION

As discussed in Chapter 1, graphene has the pseudo spin. Due to the chirality of carriers in monolayer graphene [32], weak localization is more complex than that in the 2DEG. Weak localization usually arises from the back-scattering of carriers and the

constructive interference of the wave function. Because of the Berry phase of π, anti-weak localization is expected if chiral symmetry is conserved. However, anti-localization can be suppressed by trigonal warping and intravalley scattering [38]. Furthermore conventional weak localization can be restored by elastic intervalley scattering [55] as discussed in Chapter 1.

Due to the weak localization, the correction to the change of magnetoconductivity is [15,37,38,74-76]

$$\Delta\sigma(B) = \frac{e^2}{\pi h}\left[F\left(\frac{B}{B_\phi}\right) - F\left(\frac{B}{B_\phi + 2B_i}\right) - 2F\left(\frac{B}{B_\phi + B_*}\right)\right. \tag{4.6}$$

$$F(z) = lnz + \psi(\frac{1}{2} + \frac{1}{z}),\ B_{\phi,i,*} = \frac{\hbar}{4De}\tau_{\phi,i,*}^{-1}$$

Here $\psi(z)$ is the digamma function, τ_ϕ is the phase breaking time, τ_i is the elastic intervalley scattering time, $\tau_*^{-1} = \tau_i^{-1} + \tau_w^{-1} + \tau_z^{-1}$, where τ_w is related to trigonal warping which breaks $\vec{p} \rightarrow -\vec{p}$ symmetry of the electronic dispersion and τ_z is the intravalley scattering time. D is the diffusion constant given by $D = {v_F}^2\tau/2$. τ is the transport scattering time obtained from the carrier mobility. Because of the Berry phase in monolayer graphene, the two trajectories are expected to gain a phase difference of π. However, chirality is reversed between the two valleys, thus zero phase difference between two self-intersecting trajectories is allowed in the presence of significant intervalley scattering. The first term leads to a positive magnetoconductivity if the decoherence time τ_ϕ is large.

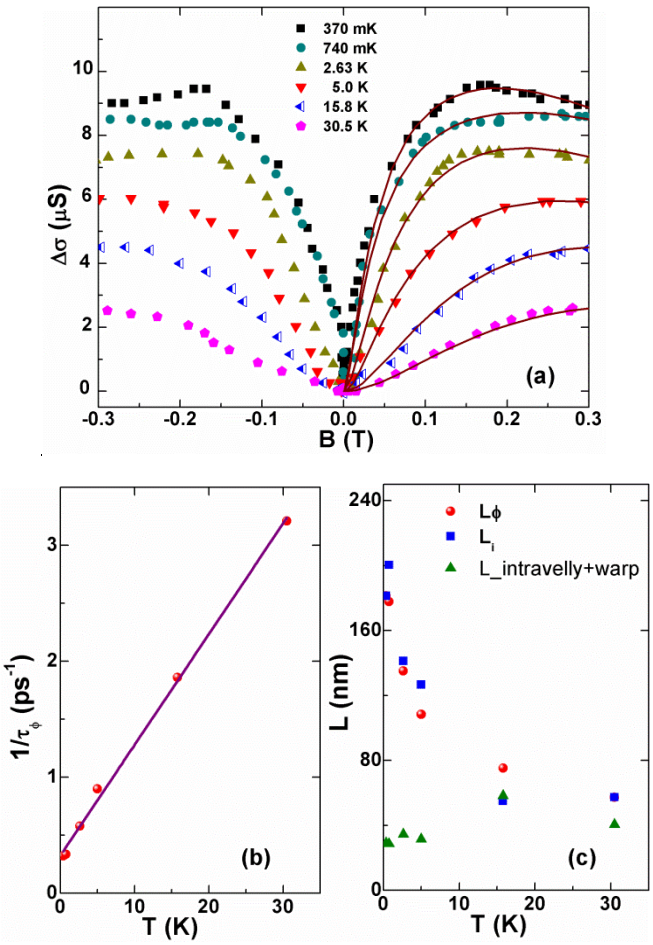

Figure 4.4 (a) The change of magnetoconductivity at low magnetic fields for a set of temperatures. (b) Inverse phase breaking time with the variation of temperature. (c) Scattering lengths as a function of temperature.

The change of magnetoconductivity $\Delta\sigma$ of our r = 50 *nm* antidot graphene is shown in Fig. 4.4(a) for a set of temperatures. At low temperature the conductivity $\Delta\sigma$ increases with rising magnetic field at low fields and then decreases above 0.15 T. At higher temperature, the conductivity monotonically increases and the value is smaller. We computed the scattering times from the best fits of experimental data to Eq. (4.6).

We find that the inelastic scattering rate is linearly proportional to temperature, $\tau_\phi{}^{-1} \propto T$, as shown in Fig. 4.4(b). The temperature dependence of τ_ϕ contains the inelastic scattering information responsible for phase breaking of charge carriers [27]. That means after coherence time τ_ϕ the wave functions which result in the constructive interference of a carrier are out of phase. This linearity has been reported by other groups and attributed to phase breaking by inelastic electron-electron scattering [15,38]. Then I calculated the phase coherence length L_ϕ, the elastic intervalley scattering length L_i and the combination of intravalley and trigonal warping scattering lengths by $L_{\phi,i,*} = \sqrt{D\tau_{\phi,i,*}}$ [39,55] for the sample with r = 50 *nm* antidots. The phase coherence length is 220 *nm* at the lowest temperature 370 mK, which is very close to the distance of nearest antidots. Interestingly, we find that the intervalley scattering length L_i for our sample is larger than phase coherence length L_ϕ. But the intravalley scattering length is much smaller than the intervalley scattering length and it is temperature independent.

4.3 ANGLE DEPENDENCE

We varied the angle θ between magnetic field and graphene surface (perpendicular direction), similar to the measurement in 2DEG of the AlInN/GaN heterostructure. Figure 4.5 shows the angle dependent resistance for r = 125 *nm* antidots at 0.37 K. At 0°, when magnetic field is perpendicular to the sample, the SdH oscillation is pronounced. When the angle is increased, the amplitude of the SdH oscillation becomes smaller. At θ = 90°, there are no oscillations. We have plotted the magnetoresistance as a function of perpendicular magnetic field $Bcos\theta$, and all the peaks collapse respectively for different

angles, as shown in Fig. 4.5(b). Hence, the behavior of carriers in graphene shows the two-dimensional nature.

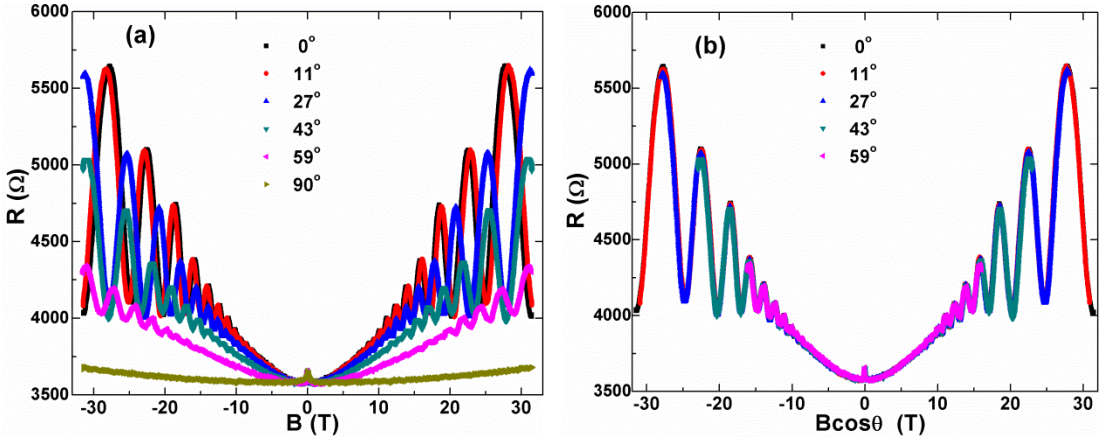

Figure 4.5 Angle dependence of magnetoresistance for graphene with antidots at T = 0.37 K. The radius of antidots is 125 *nm*.

4.4 BAND GAP

We have measured the temperature dependent resistance of our graphene samples. If there is a gap the resistance should be given by the following activation equation [77-79]

$$R = R_0 \exp(E_a / 2k_B T) \tag{4.7}$$

where E_a is the bandgap and R_0 is a constant. The Arrhenius plot is shown in Fig. 4.6. The monolayer CVD graphene without antidots has no band gap, and we can see the slope is almost zero. With the introduction of an antidot lattice, the slope of the curve is nonzero. The band gap is calculated to be (10.44 ± 0.03) *meV* for r = 50 o*nm* antidots. The bandgap for r = 125 *nm* antidots with the same nearest edge to edge distance is a little smaller, (7.918 ± 0.026) *meV*. Eroms *et al* reported a band gap around 6 *meV* with

r = 75 *nm* antidot [15]. Our results show that geometric modification using antidots is an effective method for opening a band gap in graphene.

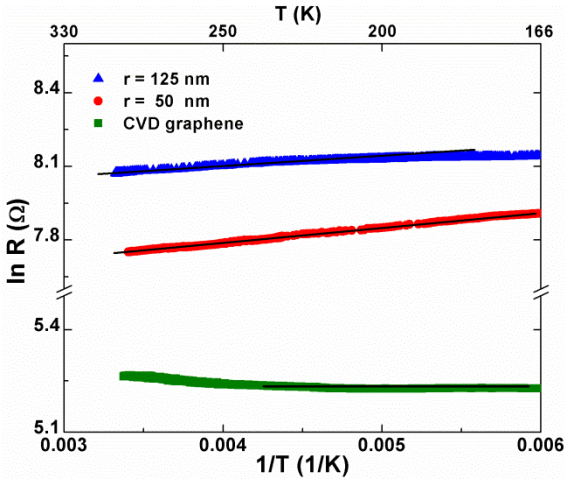

Figure 4.6 Arrhenius plot for zero-field resistance.

In conclusion, due to the linear energy dispersion relation near Dirac points, the carriers of graphene act as massless Dirac particles. We determine the effective mass $m^* = 0.087m_e$ in CVD graphene, much smaller than that in the 2DEG. Weak localization also becomes complex because of pseudo spin and nonzero Berry phase. From the weak localization effect, we find that electron-electron interaction is the dominant phase breaking mechanism. The introduction of an antidot lattice has a great influence on transport in graphene. With increasing antidot radius, Shubnikov de-Haas oscillations become more prominent, but the carrier density and effective mass are reduced. Furthermore, by tuning the antidot size, a band gap ~ 10 *meV* is obtained. The electronic properties such as carrier density, mobility, band gap can be effectively controlled by the antidot lattice.

CHAPTER 5

GEOMETRIC DEPENDENCE OF TRANSPORT IN THREE DIMENSIONAL CARBON NANOSTRUCTURES

In this chapter, three-dimensional carbon nanostructures with spherical voids have been studied. We measured the temperature dependent resistance and magnetoresistance for 4 samples with different void radii [45].

5.1 TEMPERATURE DEPENDENT RESISTANCE

The fabrication steps for our three-dimensional nanostructures have been described elsewhere [41]. Briefly, a chemical-vapor-deposition (CVD) process containing CH_4 and H_2 plasma is used to infiltrate carbon into an artificial opal substrate. After carbon infiltration, the SiO_2 spheres are etched away by dilute HF. Specimens with four different (monodispersed) voids sizes (radius r = 108 *nm*, 122 *nm*, 143 *nm* and 160 *nm*) were studied. Raman spectroscopy (JY Horiba with a HeNe laser) at room temperature is displayed in Fig. 5.1. Two prominent peaks are observed, named the D band and the G band. The intensity ratio between these two bands (I_D/I_G) is an indicator of the structural defects in the material [80,81]. All four samples have nearly the same ratio, between 1.12 and 1.16. Hence, irrespective of the void radius, these specimens are equally disordered with amorphous carbon. The dimensions of our samples range from ~ 4 *mm* × 2 *mm* × 1 *mm* to 2.5 *mm* × 1.2 *mm* × 0.5 *mm*.

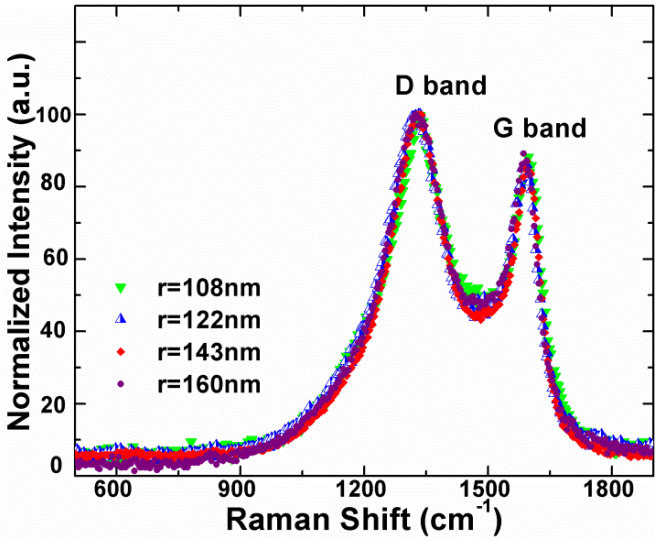

Figure 5.1 Raman spectroscopy of carbon nanostructures. All four samples show similar peaks. Reproduced from [82], with the permission of AIP publishing.

The temperature-dependent resistivity $\rho(T)$ is shown in Fig. 5.2. $\rho = RWt/L$, where R is the resistance; L, W and t are the geometric length, width and thickness of the sample respectively. Clearly, the resistivity increases with decreasing temperature. At high temperatures, $\rho(T)$ shows weak temperature dependence. Similar to the Raman data, $\rho(T)$ has almost the same value, independent of the void radius. However at low temperatures below 20 K, the resistivity increases drastically with decreasing temperature. Moreover, size dependent $\rho(T)$ is observed. For the sample with small void size, $\rho(T)$ is around 0.5 Ωcm at T =280 mK; but for the larger voids, the resistivity increases to 5 Ωcm at 280 mK. Such a large difference might indicate a metal insulator transition (MIT); one important criterion for MIT is the value of the zero-temperature conductivity $\sigma(T = 0)$. A finite $\sigma(0)$ corresponds to the metallic regime, while $\sigma(0)$ vanishes in the insulating phase [83]. In the metallic regime the conductivity can be

describe by $\sigma(T,B) = \sigma(0,B) + c(B)T^{1/2}$ [84] where $c(B)$ is a temperature independent constant. The conductivity as a function of $T^{1/2}$ for all four samples is shown in the inset of Fig. 2. The extrapolated zero-temperature intercepts, *i.e.* $\sigma(0)$, for both r =108 *nm* and 122 *nm* are finite and positive, indicating metallic behavior. In contrast samples with larger voids have negative intercepts [84,85]. Hence with increased void size, charge transport changes from metallic to insulating.

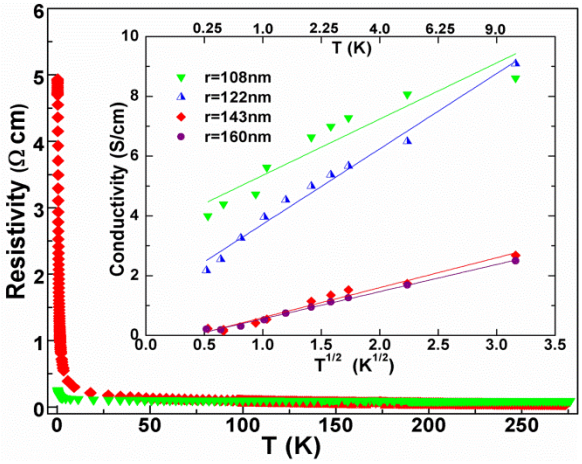

Figure 5.2 Temperature dependent resistivity of structures at zero-magnetic field. For clarity, the resistivity of only two samples is plotted. The inset is the conductivity *vs.* $T^{1/2}$ for four samples.

5.2 LINEAR MAGNETORESISTANCE AND UNIVERSAL BEHAVIOR

The magnetoresistance (MR) is defined as follows:

$$MR = [R_{xx}(B,T) - R_{xx}(0,T)]/R_{xx}(0,T) \tag{5.1}$$

where $R_{xx}(B,T)$ and $R_{xx}(0,T)$ are the resistances at magnetic field B and zero respectively. The transverse MR, *i.e.* for magnetic field (B) perpendicular to the input current ($B \perp I$), as a function of the applied magnetic field is plotted in Fig. 5.3 for the sample with r =143 *nm*. At each temperature, the MR increases with increasing magnetic field. Above 2

K, the MR is quadratic at low magnetic fields, but crosses over to a linear dependence at higher fields [80]. Interestingly, the MR remains linear and non-saturated even at 18 T, the highest field studied. At a fixed magnetic field the MR increases as temperature is decreased. However, in contrast to the behavior at high temperatures, the MR below 2 K becomes smaller at decreased temperatures. Moreover the MR in this regime saturates at high magnetic fields.

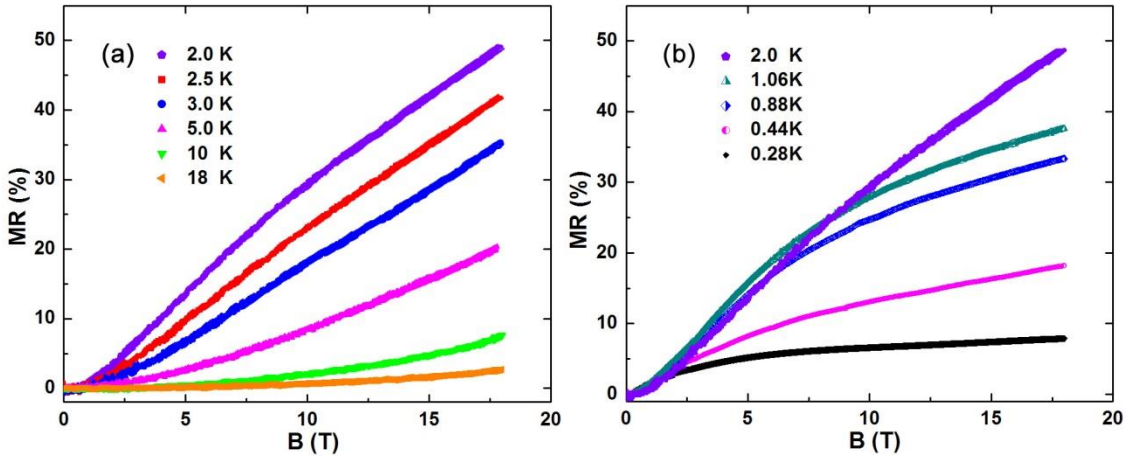

Figure 5.3 Transverse MR versus magnetic field B ($B \perp I$) at a set of temperatures for the sample with void radius r =143 *nm*.

DC Hall measurements show that the charge transport is dominated by positive holes. From the Hall voltage, the carrier density p is calculated according to $V_H = IB/(pet)$. The carrier mobility is obtained by $\mu = 1/(pe\rho)$; here I is the input current, e is the charge of the carriers, ρ is the resistivity and t is the geometric thickness of the sample. As shown in Fig. 5.4(a), the carrier density p decreases with decreasing temperature. However, the mobility displays complicated temperature dependence. As the temperature is reduced, the mobility increases until 1.06 K where it reaches a maximum, and then it decreases at lower temperatures. This single asymmetrical peak as a function of

temperature may result from two competing scattering mechanisms, such as lattice vibrations and defect scattering, which has been reported in the classic work on boron doped silicon [86] as well as black Phosphorus and the topological insulator YPtSb [87,88]. In our system the mobility is linearly proportional to the temperature below 1.06 K, whereas it is inversely proportional above 1.06 K. Fig. 5.4(b) displays the temperature dependence of the mobility; all points (T >2 K) are best described by a straight line, following $\mu(T) \propto T^{-1}$. Such temperature dependence is due to acoustic-mode phonon scattering where the relaxation time is inversely proportional to the temperature [88-91].

The slope of the linear MR, *dMR/dB*, as a function of inverse temperature is shown in Fig. 5.4(b). Remarkably this slope is also linearly proportional to inverse temperature, the same behavior as the mobility above 1.06 K. The linear increase in slope (*dMR/dB*) with the carrier mobility as evidenced in Fig. 5.4(c) validates the conjecture that slope of the linear MR is directly dependent on the mobility [92].

The significance of the carrier mobility in the linear MR is further attested by the crossover field B_{cross}. The crossover field, where the MR changes from quadratic behavior to linear behavior, is also highly temperature dependent. B_{cross} increases with temperature, which may indicate that B_{cross} is also dependent on mobility. Fig. 5.4(c) confirms our expectation because the crossover field is indeed proportional to μ. This behavior is different from the Parish and Littlewood model in highly disordered system where $B_{cross} \propto \mu^{-1}$ [93,94].

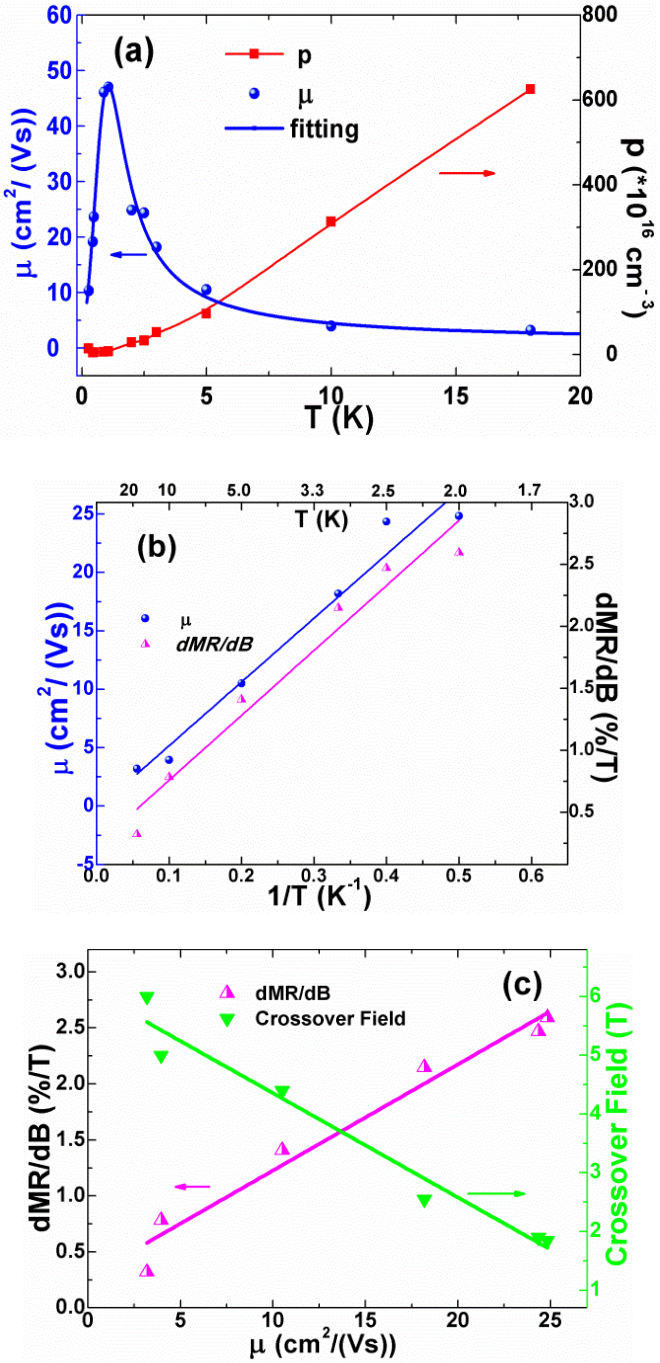

Figure 5.4 (a) Temperature dependence of carrier density and mobility for the sample with void radius r =143 nm. (b) Inverse temperature dependence of the linear slope (*dMR/dB*) and carrier mobility μ. (c) The linear dependence of slope and crossover field on mobility, validating that the MR is proportional to the mobility.

As concluded earlier, the slope is directly proportional to the mobility [92,95], hence the linear MR is given by

$$MR \propto \mu(T)B \tag{5.2}$$

Since $\mu(T) \propto T^{-1}$, we anticipate

$$MR \propto B/T \tag{5.3}$$

Consequently the linear MR will only be a function of $\xi \equiv B/T$, *i.e.* $MR = f(\xi)$. Independent of the individual values of *B* and *T*, the MR is the same as long as ξ has the same value. Therefore, a universal behavior follows and can be used to predict the magnetoresistance. MR data for *r* =143 *nm* is replotted as a function of this parameter ξ in Fig. 5.5(a). All data at different temperatures do collapse onto a single curve, indicating universal behavior. Interestingly, although this universal behavior is derived in the linear regime, universality with ξ appears to be a more general feature. As shown in Fig. 5.5(a), even in the quadratic regime MR continues to follow the universal curve.

According to Kohler's rule, if there is a single species of charge carrier and the scattering time is the same at all points on the Fermi surface, the field dependence of the MR can be rescaled to a universal function [96]

$$\frac{\Delta R}{R(0,T)} = f\left(\frac{B}{R(0,T)}\right), \text{or} = F(\mu B) \tag{5.4}$$

Where $R(0,T)$ is the zero-magnetic field resistance. The finding of universality, as evidenced in Fig. 5.5(a), indicates that a single scattering time is dominant in our sample above 2 K [97-99]. However, Kohler type scaling behavior is not observed at lower temperatures below 2 K. Such deviations may indicate the presence of additional scattering mechanisms. This can be explained from the behavior of the mobility. As discussed earlier, the mobility increases towards a maximum and then falls off with

decreasing temperature, consistent with the dominance of phonon scattering at high temperatures and emergence of surface scattering at low temperatures.

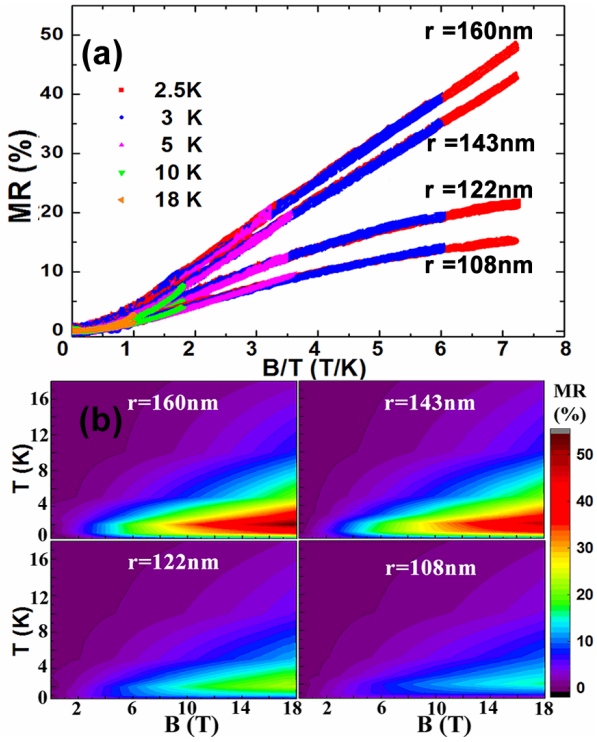

Figure 5.5 (a) Universal behavior of the MR as a function of *B/T* for all four samples, following Kohler's rule. (b) Contour plots of MR on the *B*-*T* plane as a function of magnetic field and temperature. The MR becomes larger with increased void radius.

Magnetoresistance for structures with voids of different size (*r* = 108 *nm*, 122 *nm* and 160 *nm*) show qualitatively similar temperature and field dependences as in the case of *r* =143 *nm*. As a function of temperature, the MR increases with decreasing temperature until a peak value (at about 2 K) is reached. It then falls at lower temperatures. Also the MR increases with increasing magnetic field. However the MR also displays a dependence on void size. Similar to the zero-field resistivity, the MR increases with void radius [100]. For example, at the peak (around 2 K and 18 T), the value of magnetoresistance is only 15.7% for the *r* =108 *nm* sample; it increases to 54.2% for the

largest void size (160 *nm*). It seems that the insulating phase with a large void radius has a stronger magneto response than the metallic samples. The *B*-*T* plane contour plots of peak behavior for all four sizes are shown in Fig. 5.5(b).

Universal behavior as a function of $\xi \equiv B/T$ is also observed for the other three samples. The entire experimental data fall on the respective Kohler's curves for each sample as shown in Fig. 5.5(a). Such curves show the void size dependence; in the smaller sized sample the MR is smaller. Moreover the MR becomes saturated for the samples with *r* =108 and 122 *nm* in high *B/T* region.

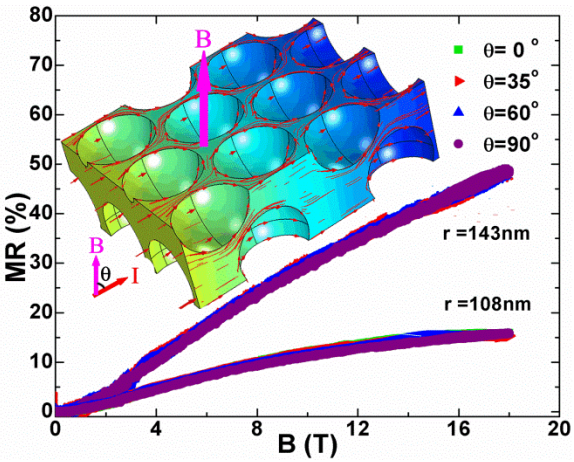

Figure 5.6 The MR at different angles at T=2 K for two samples. The inset is a schematic diagram of the microscopic current flow around the voids. The red arrow indicates that the current has components along all three Cartesian directions. Reproduced from [82], with the permission of AIP publishing.

5.3 ORIENTATION INDEPENDENCE

The orientation dependence of the MR on magnetic field was also investigated. Current is applied along the longest dimension of the sample. The resistance is measured along the current while the orientation of the sample with respect to the applied field (fixed direction) is varied by changing angle θ, as shown in the inset of Fig. 5.6.

Generally in materials where spin effects are negligible, $MR \propto sin\theta$, which is widely reported in Graphene [101], nonmagnetic metals [97] and topological insulators [102]. Interestingly, the MR in our carbon structures is independent of the angle θ. In Fig. 5.6, the MR at four different angles overlap perfectly for *r* =143 *nm* sample at 2 K. The same is true for the 108 *nm* sample. We believe this orientation independence of the MR results from the no-line of sight geometry in these structures. Because the samples are packed with voids, the charge carriers cannot flow straight between electrodes; instead they must zigzag around the voids. That is, no matter what is the direction of magnetic field, the current in the sample has to flow in all three Cartesian directions, as illustrated in the inset of Fig. 5.6. A similar conclusion was drawn by Shik [103] for transport in semiconductors with high inhomogeneity. Hence the overall transport does not change as the angle between the current and magnetic field is varied.

In summary, the magneto transport properties in 3D carbon nanostructures with an ordered lattice of spherical voids are qualitatively similar to those of materials with imperfections. A linear MR is observed. Void radius plays an important role in the zero-field resistance and in the MR. By increasing the void size, the material is tuned from metal to insulator; the MR is also enhanced. Interestingly the MR displays distinct high and low temperature behavior. At high temperatures the mobility is inversely proportional to the temperature and controls magneto transport; in this regime, the MR exhibits a Kohler type universal behavior with B/T. Furthermore, the MR is insensitive to the relative orientation between the magnetic field and the direction of the bulk current flow.

Linear MR even at high magnetic fields coupled with insensitivity to orientation is an interesting combination that may be useful in omnidirectional magnetic field detectors.

CHAPTER 6

CONCLUSION

Electrical and magneto transport properties have been investigated in three types of systems: Graphene, Two-dimensional electron gas (2DEG) in AlInN/GaN heterostructures and 3D carbon nanostructures with spherical voids.

AlInN is the newest and amongst the widest band gap semiconductors. We report the first observation of weak localization in the 2DEG of a AlInN/GaN heterostucture. This is confirmed by the *lnT* dependence of the zero-field conductivity and angle dependence of magnetoresistance. We demonstrate that electron-electron scattering is the principal phase breaking mechanism. Furthermore, the Shubnikov-de Haas (SdH) oscillation is studied in this system, and is consistent with the conventional 2DEG behavior. The effective mass of the electron is found to be $0.2327m_e$.

Graphene, a single layer of carbon atoms, has an unconventional linear energy dispersion relation near the Dirac points. We determine the effective mass to be $0.087m_e$ in CVD graphene, much smaller than that in the 2DEG. Due to the pseudo spin and chirality we find weak localization is more complex than in the 2DEG in AlInN/GaN. Furthermore, the antidot lattice has great influence on the properties of graphene; it can effectively change the carrier density and effective mass by tuning antidot size. In addition, a band gap ~ 10 *meV* is obtained by such geometric manipulations.

The magneto response observed in graphene and the 2DEG is sensitive to the orientation between the applied magnetic field and input current, showing the two-dimensional nature of carriers. However, we find that orientation-independent magnetoresistance can be achieved in three-dimensional carbon nanostructures with spherical voids. Moreover, non-saturating linear magnetoresistance in such system is observed, and the magnitude can be enhanced by increasing void size. Linear magnetoresistance coupled with orientation insensitivity is an interesting combination for omnidirectional magnetic field detectors.

The study of these three materials concludes that the structure difference of system affects the energy dispersion relation, which gives rise to various physical properties. By manipulating the geometric parameters, we can effectively tune the electronic properties of the systems.

REFERENCES

[1] K. S. Novoselov, A. K. Geim, S. V. Morozov, D. Jiang, M. I. Katsnelson, I. V. Grigorieva, S. V. Dubonos, and A. A. Firsov, Nature **438**, 197 (2005).

[2] Y. Zhang, Y.-W. Tan, H. L. Stormer, and P. Kim, Nature **438**, 201 (2005).

[3] A. K. Geim and K. S. Novoselov, Nature Materials **6**, 183 (2007).

[4] S. J. Pearton, J. C. Zolper, R. J. Shul, and F. Ren, J. Appl. Phys. **86**, 1 (1999).

[5] A. F. Braña, C. Diaz-Paniagua, F. Batallan, J. A. Garrido, E. Muñoz, and F. Omnes, J. Appl. Phys. **88**, 932 (2000).

[6] R. Butte *et al.*, J. Phys. D: Appl. Phys. **40**, 6328 (2007).

[7] B. Q. Lv *et al.*, Phys. Rev. X **5**, 031013 (2015).

[8] S.-Y. Xu *et al.*, Science **349**, 613 (2015).

[9] H. Cao, J. Tian, I. Miotkowski, T. Shen, J. Hu, S. Qiao, and Y. P. Chen, Phys. Rev. Lett. **108**, 216803 (2012).

[10] D. X. Qu, Y. S. Hor, J. Xiong, R. J. Cava, and N. P. Ong, Science **329**, 821 (2010).

[11] A. H. C. Neto, F. Guinea, N. M. R. Peres, K. S. Novoselov, and A. K. Geim, Rev. Mod. Phys. **81**, 109 (2009).

[12] W. Xua and T.-W. Lee, Mater. Horiz. **3**, 186 (2016).

[13] G. Liu *et al.*, ACS Nano **6**, 6786 (2012).

[14] Z. Fan, A. Uppstu, and A. Harju, Phys. Rev. B **91**, 125434 (2015).

[15] J. Eroms and D. Weiss, New Journal of Physics **11**, 095021 (2009).

[16] N. W. Ashcroft and N. D. Mermin, *Solid State Physics* (Thomson Learning, Inc, 1976).

[17] J. M. Ziman, *Electrons and Phonons* (Oxford University Press, Clarendon, 1962).

[18] Y. M. Galperin, (Lund University, 1998), p. 131.

[19] M. S. Dresselhaus, in *Transport Properties of Solids* (Massachusetts Institute of Technology, 2001), p. 228.

[20] M. Lachab, M. Sultana, Q. Fareed, F. Husna, V. Adivarahan, and A. Khan, J. Phys. D: Appl. Phys. **47**, 135108 (2014).

[21] X. He, D. Zhao, and D. Jiang, Chin. Phys. B **24**, 067301 (2015).

[22] O. Ambacher *et al.*, J. Appl. Phys. **87**, 334 (2000).

[23] J.-N. Fuchs, (UPMC, Paris, 2013).

[24] T. Izraeli, (Israel Institute of Technology, 2012).

[25] T. Osada, J. Phys. Soc. Jpn. **77**, 084711 (2008).

[26] B. Grbic, R. Leturcq, T. Ihn, K. Ensslin, D. Reuter, and A. D. Wieck, Phys. Rev. B **77**, 125312 (2008).

[27] S. McPhail, C. E. Yasin, A. R. Hamilton, M. Y. Simmons, E. H. Linfield, M. Pepper, and D. A. Ritchie, Phys. Rev. B **70**, 245311 (2004).

[28] Z. J. Qiu, Y. S. Gui, T. Lin, N. Dai, J. H. Chu, N. Tang, J. Lu, and B. Shen, Phys. Rev. B **69**, 125335 (2004).

[29] R. G. Wheeler, Phys. Rev. B **24**, 4645 (1981).

[30] M. S. Dresselhaus and E. McCann, *Graphene Nanoelectronics Metrology, Synthesis, Properties and Application* (Springer-Verlag Berlin Heidelberg, 2012).

[31] P. Kim, (Columbia University, 2011), p. 20.

[32] E. McCann, Physics **2**, 98 (2009).

[33] M. V. Berry, Proc. R. Soc. Lond. A **392**, 45 (1984).

[34] C. G. Torre, (Utah State University, 2007), p. 5.

[35] R. Saito, G. Dresselhaus, and M. S. Dresselhaus, Phys. Rev. B **61**, 2981 (200).

[36] D.-K. Ki, D. Jeong, J.-H. Choi, H.-J. Lee, and K.-S. Park, Phys. Rev. B **78**, 125409 (2008).

[37] E. McCann, K. Kechedzhi, V. I. Fal'ko, H. Suzuura, T. Ando, and B. L. Altshuler, Phys. Rev. Lett. **97**, 146805 (2006).

[38] F. V. Tikhonenko, A. A. Kozikov, A. K. Savchenko, and R. V. Gorbachev, Phys. Rev. Lett. **103**, 226801 (2009).

[39] A. M. R. Baker *et al.*, Phys. Rev. B **86**, 235441 (2012).

[40] A. C. Ferrari *et al.*, Phys. Rev. Lett. **97**, 187401 (2006).

[41] A. A. Zakhidov, R. H. Baughman, Z. Iqbal, C. X. Cui, I. Khayrullin, S. O. Dantas, J. Marti, and V. G. Ralchenko, Science **282**, 897 (1998).

[42] I. Gorczyca, T. Suski, N. E. Christensen, and A. Svane, Phys. Rev. B **93**, 165302 (2016).

[43] E. A. Henriksen, S. Syed, Y. Ahmadian, M. J. Manfra, K. W. Baldwin, A. M. Sergent, R. J. Molnar, and H. L. Stormer, Appl. Phys. Lett. **86**, 252108 (2005).

[44] R. Tülek, A. Ilgaz, S. Gökden, A. Teke, M. K. Öztürk, M. Kasap, S. Özçelik, E. Arslan, and E. Özbay, J. Appl. Phys. **105**, 013707 (2009).

[45] L. Z. Wang, M. Yin, J. Jaroszynski, Ju-HyunPark, G. Mbamalu, and T. Datta, Appl. Phys. Lett. **109**, 123104 (2016).

[46]S. B. Lisesivdin, A. Yildiz, N. Balkan, M. Kasap, S. Ozcelik, and E. Ozbay1, J. Appl. Phys. **108**, 013712 (2010).

[47] Z. L. Miao *et al.*, J. Appl. Phys. **109**, 016102 (2011).

[48] M. B. Shalom, A. Ron, A. Palevski, and Y. Dagan, Phys. Rev. Lett. **105**, 206401 (2010).

[49] A. D. Caviglia, S. Gariglio, C. Cancellieri, B. Sacépé, A. Fête, N. Reyren, M. Gabay, A. F. Morpurgo, and J.-M. Triscone, Phys. Rev. Lett. **105**, 236802 (2010).

[50]A. Bayraklı, E. Arslan, T. Fırat, Ş. Özcan, Ö. Kazar, H. Çakmak, and E. Özbay, Phys. Status. Solidi A **209**, 1119 (2012).

[51] E. Frayssinet *et al.*, Appl. Phys. Lett. **77**, 2551 (2000).

[52] P. T. Coleridge, Phys. Rev. B **44**, 3793 (1991).

[53]M. J. Manfra, S. H. Simon, K. W. Baldwin, A. M. Sergent, K. W. West, R. J. Molnar, and J. Caissie, Appl. Phys. Lett. **85**, 5278 (2004).

[54] S. Hikami, A. I. Larkin, and Y. Nagaoka, Prog. Theor. Phys. **63**, 707 (1980).

[55]F. V. Tikhonenko, D. W. Horsell, R. V. Gorbachev, and A. K. Savchenko, Phys. Rev. Lett. **100**, 056802 (2008).

[56] J. J. Lin and J. P. Bird, J. Phys.: Condens. Matter **144**, 501 (2002).

[57] K. K. Choi, D. C. Tsui, and K. Alavi, Phys. Rev. B **36**, 7751 (1987).

[58] G. Du, V. N. Prigodin, A. Burns, J. Joo, C. S. Wang, and A. J. Epstein, Phys. Rev. B **58**, 4485 (1998).

[59] D. Hoadley, P. McConville, and N. O. Birge, Phys. Rev. B **60**, 5617 (1999).

[60] Z. J. Qiu, Y. S. Gui, T. Lin, J. Lu, N. Tang, B. Shen, N. Dai, and J. H. Chu, Solid State Commun. **131**, 37 (2004).

[61] Y. Zhang, T.-T. Tang, C. Girit, Z. Hao, M. C. Martin, A. Zettl, M. F. Crommie, Y. R. Shen, and F. Wang, Nature **459**, 820 (2009).

[62] S. Yuan, Rafael Roldan, A.-P. Jauho, and M. I. Katsnelson, Phys. Rev. B **87**, 085430 (2013).

[63] T. G. Pedersen, C. Flindt, J. Pedersen, N. A. Mortensen, A.-P. Jauho, and K. Pedersen, Phys. Rev. Lett. **100**, 136804 (2008).

[64] F. Ouyang, S. Peng, Z. Liu, and Z. Liu, ACS Nano **5**, 4023 (2011).

[65] A. Sandner, T. Preis, C. Schell, P. Giudici, K. Watanabe, T. Taniguchi, D. Weiss, and J. Eroms, Nano Lett. **15**, 8402 (2015).

[66] K. Zou, X. Hong, and J. Zhu, Phys. Rev. B **84**, 085408 (2011).

[67] J. Jobst, D. Waldmann, F. Speck, R. Hirner, D. K. Maude, T. Seyller, and H. B. Weber, Phys. Rev. B **81**, 195434 (2010).

[68] H. Hirai, H. Tsuchiya, Y. Kamakura, N. Mori, and M. Ogawa, J. Appl. Phys **116**, 083703 (2014).

[69] A. Lartsev, T. Yager, T. Bergsten, A. Tzalenchuk, T. J. B. M. Janssen, R. Yakimova, Samuel Lara-Avila, and S. Kubatkin, Appl. Phys. Lett. **105**, 063106 (2014).

[70] K. I. Bolotin, K. J. Sikes, Z. Jiang, M. Klima, G. Fudenberg, J. Hone, P. Kim, and H. L. Stormer, Solid State Comm. **146**, 351 (2008).

[71] E. Tiras, S. Ardali, T. Tiras, E. Arslan, S. Cakmakyapan, O. Kazar, J. Hassan, E. Janzen, and E. Ozbay, J. Appl. Phys **113**, 043708 (2013).

[72] J. Li, L. Z. Tan, K. Zou, A. A. Stabile, D. J. Seiwell, K. Watanabe, T. Taniguchi, S. G. Louie, and J. Zhu, Phys. Rev. B **94**, 161406 (2016).

[73] X. Hong, K. Zou, and J. Zhu, Phys. Rev. B **80**, 241415 (2009).

[74] R. V. Gorbachev, F. V. Tikhonenko, A. S. Mayorov, D. W. Horsell, and A. K. Savchenko, Phys. Rev. Lett. **98**, 176805 (2007).

[75] K. Kechedzhi, V. I. Fal'ko, E. McCann, and B. L. Altshuler, Phys. Rev. Lett. **98**, 176806 (2007).

[76] S. V. Morozov, K. S. Novoselov, M. I. Katsnelson, F. Schedin, L. A. Ponomarenko, D. Jiang, and A. K. Geim, Phys. Rev. Lett. **97**, 016801 (2006).

[77] T. Khodkov, I. Khrapach, M. F. Craciun, and S. Russo, Nano Lett. **15**, 4429 (2015).

[78] M. Kim, N. S. Safron, M. S. A. Eungnak Han, and P. Gopalan, Nano Lett. **10**, 1125 (2010).

[79] T. Shimizu, J. Haruyama, D. C. Marcano, D. V. Kosinkin, J. M. Tour, K. Hirose, and K. Suenaga, Nat. Nanotechnol. **6**, 45 (2011).

[80] L. Z. Wang, M. Yin, M. Abdi, and T. Datta, Appl. Phys. Lett. **107**, 023103 (2015).

[81] L. Z. Wang, H. Wang, T. Datta, M. Yin, and X. Y. Tian, J. Appl. Phys. **116**, 173708 (2014).

[82] L. Wang, M. Yin, J. Jaroszynski, J.-H. Park, G. Mbamalu, and T. Datta, Appl. Phys. Lett. **109**, 123104 (2016).

[83] D. M. Basko, I. L. Aleiner, and B. L. Altshuler, Ann. Phys. **321**, 1126 (2006).

[84] T. Wojtowicz, T. Dietl, M. Sawicki, W. Plesiewicz, and J. Jaroszynski, Phys. Rev. Lett. **56**, 2419 (1986).

[85] S. Bogdanovich, P. H. Dai, M. P. Sarachik, and V. Dobrosavljevic, Phys. Rev. Lett. **74**, 2543 (1995).

[86] G. L. Pearson and J. Bardeen, Phys. Rev. **75**, 865 (1949).

[87] C. Shekhar, S. Ouardi, A. K. Nayak, G. H. Fecher, W. Schnelle, and C. Felser, Phys. Rev. B **86**, 155314 (2012).

[88] Z. P. Hou *et al.*, Sci. Rep. **6**, 23807 (2016).

[89] S. H. Zhang, W. Xu, S. M. Badalyan, and F. M. Peeters, Phys. Rev. B **87**, 075443 (2013).

[90] E. E. Mendez, P. J. Price, and M. Heiblum, Appl. Phys. Lett. **45**, 294 (1984).

[91] J. M. Ziman, *Electrons and Phonons: The Theory of Transport Phenomena in Solids* (Oxford University Press, London, 1962), p. 434.

[92] H. G. Johnson, S. P. Bennett, R. Barua, L. H. Lewis, and D. Heiman, Phys. Rev. B **82**, 085202 (2010).

[93] M. M. Parish and P. B. Littlewood, Nature **426**, 162 (2003).

[94] M. M. Parish and P. B. Littlewood, Phys. Rev. B **72**, 094417 (2005).

[95] C. Shekhar, S. Ouardi, G. H. Fecher, A. K. Nayak, C. Felser, and E. Ikenaga, Appl. Phys. Lett. **100**, 252109 (2012).

[96] A. B. Pippard, *Magnetoresistance in Metals* (Cambridge University Press, Cambridge, 1989), p. 23.

[97] H. Takatsu, J. J. Ishikawa, S. Yonezawa, H. Yoshino, T. Shishidou, T. Oguchi, K. Murata, and Y. Maeno, Phys. Rev. Lett. **111**, 056601 (2013).

[98] S. Ishiwata, Y. Shiomi, J. S. Lee, M. S. Bahramy, T. Suzuki, M. Uchida, R. Arita, Y. Taguchi, and Y. Tokura, Nat. Mater **12**, 512 (2013).

[99] E. Mun, H. Ko, G. J. Miller, G. D. Samolyuk, S. L. Bud'ko, and P. C. Canfield, Phys. Rev. B **85**, 035135 (2012).

[100] H. Take, T. Matsumoto, S. Hiwatashi, T. Nakayama, K. Niihara, and K. Yoshino, Jpn. J. Appl. Phys. **43**, 4453 (2004).

[101] R. S. Singh, X. Wang, W. Chen, A. Andrew, and T. S. Wee, Appl. Phys. Lett. **101**, 183105 (2012).

[102] J. Lee, J. Park, J. H. Lee, J. S. Kim, and H. J. Lee, Phys. Rev. B **86**, 245321 (2012).

[103] A. Y. Shik, *Electronic Properties of Inhomogeneous Semiconductors* (CRC Press, 1995), Vol. 9, p. 56.

APPENDIX A

FABRICATION OF GRAPHENE WITH AN ANTIDOT LATTICE

The procedures to pattern antidots on graphene are shown in Fig. A.1. They include:

1. Spin coating the positive resist (PMMA 950k) on graphene using a spinner at 4000 rpm for 60 sec. The thickness of resist is around 300 *nm*. Repeat again so that the resist is thick enough. After that, put the sample on the hotplate at 150 °C for 90 sec.
2. Electron beam lithography. Load the sample into the chamber of the JOEL JSM 840A Scanning Microscope. Pump the chamber to 20mT. Control the electron beam gun using a write program to pattern the antidots.
3. Development. After the desired regions are exposed by the electron beam, develop the sample using MIBK: IPA=1:3 for 30 sec at 23 °C, then flush using IPA for 40 sec. Observe the antidots using an optical microscope; if the pattern is not clear, do the development a little longer. Then bake the sample again at 150 °C for 60 sec.
4. Etch graphene using O_2 plasma. The antidot lattice has been formed on resist. Now we need to transfer these antidots to graphene. Using the oxygen plasma, the carbon atoms which are not covered by resist can be removed. Put the sample into the chamber of Phantom Reactive Ion Etch (Trion Technology). Set up the

pressure as 100 mT, ICP power as 50 W, RIE power 50 W and O_2 flow 90 sccm. The etching time is 11 sec. Check the pattern after O_2 etching using the optical microscope.

So far the antidots have been formed. Next we are going to do the second-step lithography and deposit Ti/Au contacts.

5. Electron beam lithography to pattern contacts on graphene. Spin coat the graphene using resist PMMA 950k. Put the sample in the chamber of SEM again; pattern the contact using electron gun.
6. Development, the same as step 3.
7. Deposit the Ti/Au thin films using electron beam deposition. Load the sample and pump to vacuum $\sim 2 \times 10^{-6}\,\mathrm{Torr}$. The voltage of electron gun is 4.79 kV. Increase the current to 84 mA, deposit 10 *nm* Titanium (Ti) at the rate around 0.3 $\text{Å}/\text{s}$. Then change to the gold (Au) source; start deposition at a current ~ 88 mA and deposition rate 0.7 $\text{Å}/\text{s}$. The thickness of Au is 60 *nm*.
8. Lift off. Put the sample into acetone, waiting for 45 min until the undesired pattern is moved away from the substrate.

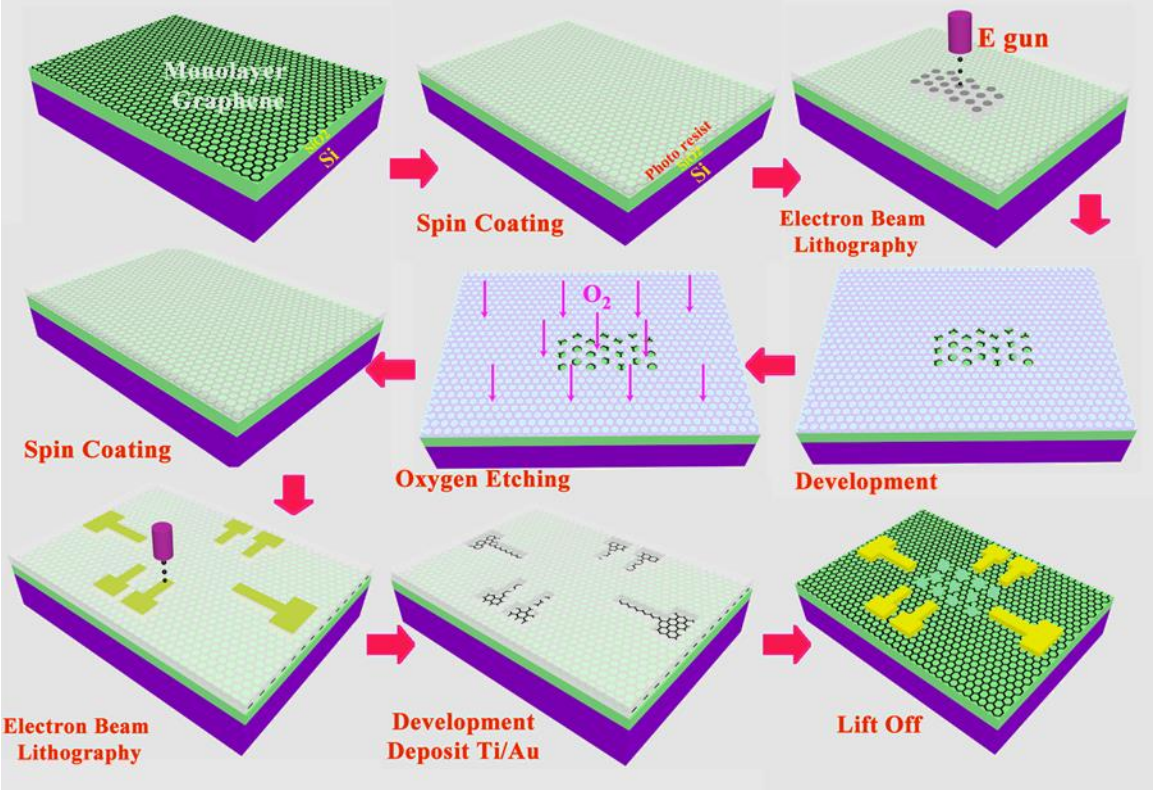

Figure A.1 Schematic diagrams of fabrication procedures using electron beam lithography, reactive ion etch and electron gun deposition.

The antidot pattern is designed using DesignCAD. There are four layers in total as shown in Fig. A.2. Layer 1 is a hexagonal array of antidots, with the radius of antidot r =125 *nm*. Layers 2 and 3 are the mesas to isolate the graphene with other regions. Layer 4 is the contact pattern. Each layer is written separately with the corresponding magnification using electron beam lithography.

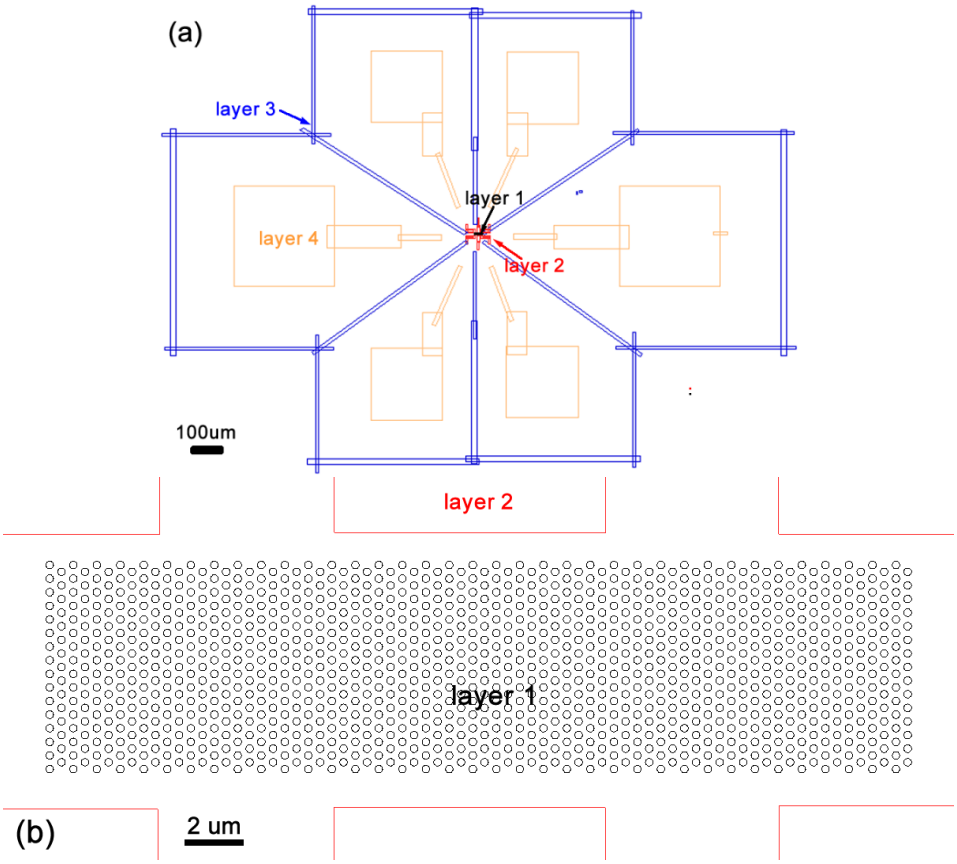

Figure A.2 Antidot pattern design. (a) All 4 layers, labeled using different colors. Black region is layer 1, layer 2 is red region, layer 3 is blue region and layer 4 is orange region. (b)Zoom-in image of layer 1 with antidot array. It is a hexagonal lattice of antidots.

APPENDIX B

FABRICATION OF AN ALINN/GAN HALL BAR

The procedures to fabricate the AlInN/GaN Hall bar include:

1. Clean the wafer. Put the AlInN/GaN wafer in Acetone/IPA hot bath for 3 min, then spray the wafer using IPA and blow to dry the sample using N_2 gas. Put the wafer in the HCl/HNO_3 = 3:1 for 2 min. Finally clean the acid using DI water for 5 min then dry the wafer.
2. Coat photo resist. Spin coating S1813 resist at 4000 *rpm* for 45 sec. Then bake the wafer at 85 °C for 5 min.
3. Mesa lithography. Clean the mask using Acetone/IPA and load dry mask in the Karl Suss MJB3 Mask Aligner. Expose the sample using HP mode for 8 sec with intensity13 mW/cm^2.
4. Image reversal. Put the wafer in the oven with NH_3 gas at 90 °C for 30 min. Then expose again without mask for 18 sec using Mask Aligner.
5. Develop. Put the wafer in the developer for 45 sec; then clean it using DI water for 5 min. Blow dry using N_2. Put it on the hot plate to bake again for 5 min at 85 °C.
6. Etch the wafer. Using the inductive coupled Cl_2/BCl_3 plasma to etch the wafer. Remove the resist by Acetone. Check the mesa using the optical microscope.

So far the mesa of Hall bar has been finished. Next parts are to fabricate the Ohmic contacts.

7. Coat the photo resist again as in step 2. Clean the wafer if needed.
8. Ohmic lithography. Load the Ohmic contacts mask. Expose the wafer using HP mode for 8 sec with intensity13 mW/cm^2.
9. Image reversal and develop again.
10. Deposit the Ti/Al/Ti/Au thin films. Using the electron beam deposition to deposit the thin film. The first layer is Ti with thickness of 40 *nm*, then 120 *nm* Al, then Ti with 40 *nm* again; the last layer is 80 *nm* Au.
11. Lift off. Put the wafer in Acetone for 30 min to remove the photo resist and undesired thin film. Wash it using DI water for 5 min.
12. Anneal. Put the sample in the oven and open the N_2 gas valve. Set the temperature at 850°C. Wait for 30 sec to make the Al to diffuse to the 2DEG region.

The last parts are to fabricate the contact probes.

13. Coat the photo resist and do lithography with smaller contacts mask.
14. Deposit Ti/Au. Using the electron beam deposition to deposit the Ti/Au with thickness 10/80 nm. After that lift off and clean the sample.

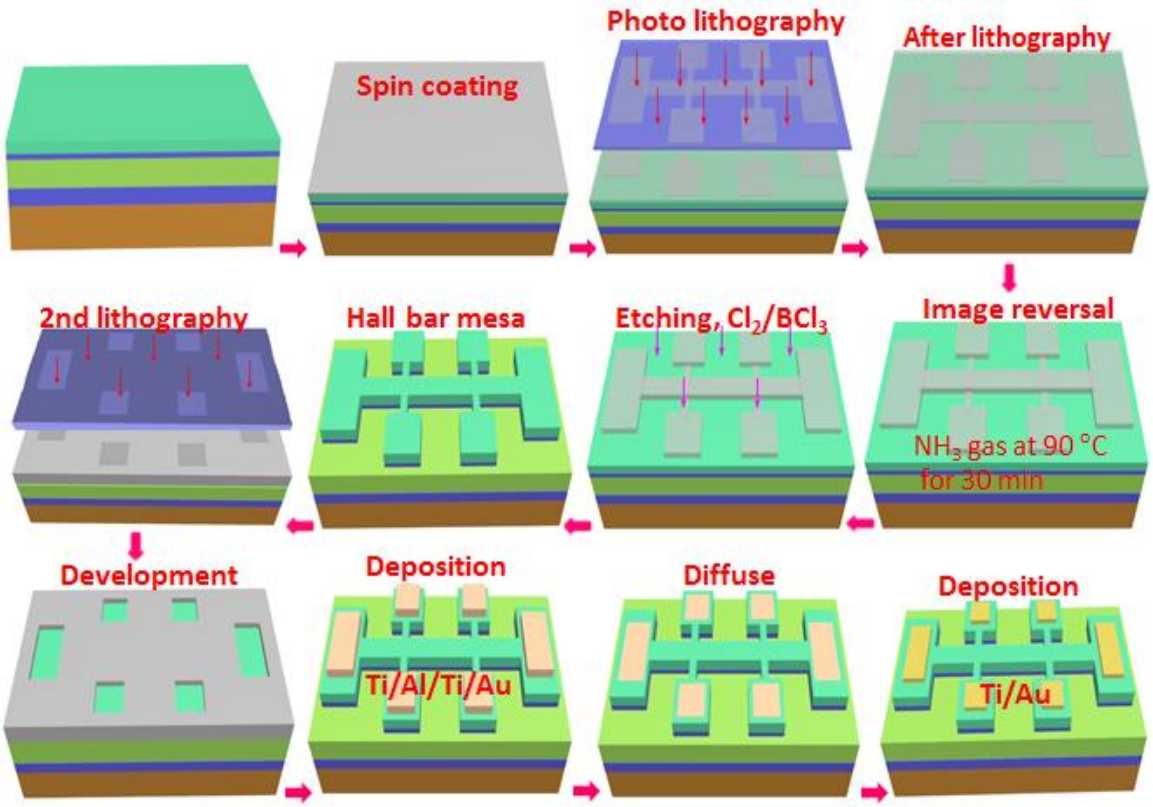

Figure B.1 Schematic diagrams of procedures to fabricate a Hall bar in AlInN/GaN heterostructure.

APPENDIX C

OPERATION MANUALS

Electron Beam Lithography

The lithography machine is a JEOL_JSM_840A Scanning Microscope combined with writing software. Below is the operation of electron beam lithography:

1. Load the sample. Check the sample stage position first, X: 25.0, Y: 35.0, Working Distance: 39. Put the sample onto the holder. Insert the sample rod to the end of chamber, with the disk firmly seated on the open end. Push the EVAC/VENT button to evacuate the chamber. Wait until the light goes off in about 1 minute. Press V7 under the table then open the gate valve. Slowly push the sample into stage. Unscrew the rod counterclockwise and then pull it to the door. Close gate valve and press V7 again. Finally Push EVAC/VENT red light button. The loading of sample is done.
2. Turn on SEM. Press ACCEL VOLTAGE to turn on SEM. Check the light of HEAT/PREHEAT and make sure it is on. The FILAMENT current is 150 mA. Increase the voltage to 30 kV; then increase the filament current slowly and check the pressure at same time until to the maximum current ~260 mA. Wait for one hour to warm up the filament.

3. Move the work distance to 8 *mm*. Switch the Detector button to SEI, PMT to ON, COLLECTOR to ON and BEAM BLANKING to EXT. Turn on the digital to analog converter.
4. Turn on the 'SEM_write' software and Open the .lay file.
5. Press G and O on the keyboard to move sample to O hole. Adjust FOCUS to get the clear image.
6. Change the PROBE CURRENT to different values and record the real current on the current meter. Change GUN ALIGNMENT to modify if the current is too small.
7. Make Spot. First move the sample to the edge. Change FOCUS to get the clear image. Increase the MAGNIFICATION to 100 000X. Turn off PCD and EXT SCAN, press SPOT button on SCAN MODE. Wait for 1 min or more until the BRIGHTNESS change to green from red. Press PIC to check the spot we got. Move the sample and repeat SPOT until the spot is clear and circular.
8. Write the pattern. Set up the current, for example 10 pA; set magnification according to the size of pattern, turn off RDC, click write and press "Yes, write."

   Because: Dose × Area = Current × time

   $$C/cm^2 \times cm^2 = \text{Ampere} \times s$$

   Here Charge dose is usually ~ 3.8 pC/um^2. So the writing time can be estimated.

9. Write layer 2, 3 and 4 if needed.
10. Shut down the SEM. Change the work distance to 39 *mm*. Press Home. Switch Detector to off, PMT to off, COLLECTOR to off and BEAM BLANKING to off.

Turn off the Digit to Analog Converter. Switch the Magnification to Maximum 300 000X, and Probe Current to Minimum. Reduce the FILAMENT Current to 150 mA and Voltage to 0 kV. Switch ACCEL VOLTAGE to Off.

11. Unload the sample from the chamber.

Electron Beam Deposition

The Ti/Au thin film is deposited by electron beam evaporation machine. Here are the operation procedures:

1. Press 'Chamber Vent', wait for 30 Sec then open the chamber.
2. Check the metal source in four boats by clicking 'CW' in EV-CI Indexer panel.
3. Mount the sample to the sample holder. Check Shutter is working or not by 'Shutters, Substr'.
4. Close the door when everything is ok. Turn on 'Vacuum' to pump the chamber. Then turn on the chiller of Turbo.
5. Wait for 2 hours to reach the vacuum around 10^{-6} Torr. Check the pressure by clicking 'EMIS' and record the value.
6. Turn on the Electron Beam Supply.
   (a) Click on 'Main', check the 'Emission Current Adjust' is on Zero. (b) Press 'High Voltage ON', then 'High Voltages' should show the value (4.8 kV usually). (c) Press 'FIL ON/OFF'.
7. Select the target metal such as Ti 'Pocket' in 'EV-CI Indexer' by click 'CW'.
8. Choose the program.

(a) Click ‘Program’ and rotate the knob to choose the desired metal target. Ti is 9. Au is 5.

(b) Press ‘Next’ to check Density, Z-Ratio and Tooling Factor. Ti: Density is 4.5 g/cm3, Z ratio is 0.628, Tooling factor for E gun method is 215%. Au: Density 19.3 g/cm3, Z ratio is 0.381.

9. Turn on Mini Sweep ‘Power’ and ‘On’ of Sweep Status to control electron beam.
10. Increase current slowly and check the target to make sure electron hit the target. Ti: 75 mA, 0.5A/sec. Au: 65 mA, 0.4A/sec.
11. Deposit the film by turning on ‘Shutter’ and press “Zero”. Record the current and deposition rate.
12. Close ‘shutter’ to bottom when thickness is ok. Reduce the current to 0 and click ‘OFF’
13. Choose another metal target such as Au by ‘CW’ ‘Pocket’ and check ‘Program’. Deposit again following the previous procedures.
14. Decrease the current to 0 and turn off “FIL ON/OFF”. Turn off Mini Sweep by ‘OFF’ and Power ‘OFF’.
15. Press “High Voltage OFF” and wait until the voltage drops to 0. Then Switch Main to OFF.
16. Turn off “Vacuum” and click Zero. Wait for 30 min to vent the chamber.
17. Press ‘Vent’ and open the chamber.
18. Remove the sample from the sample holder.
19. Close the chamber and ‘vacuum’ for a while and then Turn off the chiller.

Trion Phantom II Reactive Ion Etcher

When the antidots are patterned by electron beam lithography, the exposed graphene region will be etched away by oxygen plasma using reactive ion etch. Here are the procedures for operation of this machine:

1. Press 'Pump' and then 'Main' power. Check the pressure of N_2 gas.
2. Press 'Vent Reactor' to vent the chamber and open the lid. Load samples on to the main chamber chuck. Then press "Close Lid" to close the chamber.
3. Click 'Download Recipe' and then 'Load/Edit Recipe'.
4. Set up the desired Recipe Parameters. For example, Pressure 100 mT, ICP RF 50 W, RIE RF 50 W, O_2 gas flow 90 sccm. Click 'Exit' when done. Press 'Download Recipe'. Parameters are shown in Fig. C.1.
5. Press 'Manual Process Control'. Press the 'Vacuum Closed' button and then 'Press Iso Closed'.
6. Once pumped down to 2 mT, the 'Gases off' will appear. Make sure the O_2 gas valve of the cylinder is open. Press it and it becomes 'Gases On'.
7. Press the 'RF Off' button to toggle it to 'RF On'. This will start the process and the pink plasma glowing can be observed.
8. The timer will count upwards and click 'RF On' to stop. The etching time for monolayer graphene is around 11 sec.
9. Press 'Gases On', then 'Press Iso Open' and 'Vacuum Open'. Press 'Exit' at the end.
10. Press 'Vent Reactor' to unload the samples.
11. Turn off the machine by pressing 'Exit' and 'OFF' button.

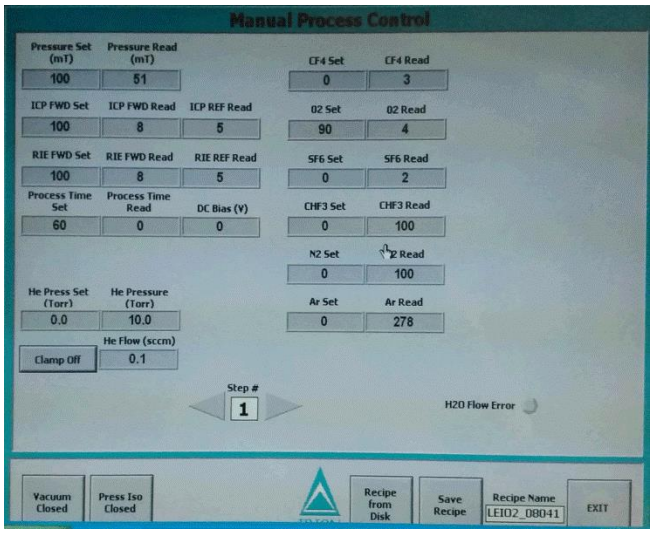

Figure C.1 Etch parameters setup for Trion Phantom II Reactive Ion Etcher.

Karl Suss MJB3 Mask Aligner

The Hall bar mesa and Ohmic contacts are patterned by photolithography using Karl Suss MJB3 Mask Aligner. The operation procedures include:

1. Check the compressed air pressure, turn on the vacuum pump.
2. Power up the lamp controller, Start the arc lamp by pressing the start button. Wait 15 min for the lamp to warm up.
3. Power on the Mask Aligner by pressing the red POWER button on the control panel. Turn on the microscope.
4. Load the mask. Mount the photo-mask on the mask holder and make sure the chrome side of the mask is facing up, close to the wafer.

5. Press the VACUUM MASK button on the control panel and check that the mask is securely attached to the holder. Pick up the mask holder and flip it over. Insert it into the mask holder grooves and tighten the knobs on the front.
6. Load the wafer. Place the sample on the sample holder and verify that all vacuum holes are covered.
7. While viewing through the microscope, gently move the Contact Lever counter-clockwise on the left-hand side of Mask Aligner. The Separation Lever cannot be used unless the Contact lever is pushed into contact position.
8. Move the Separation lever to the front of the tool. The SEPAEARION indicator light on the control panel will illuminate and the CONTACT light will power off.
9. Focus the microscope. Align the substrate using the X, Y and θ position micrometers. When done, move the Separation Lever backwards to move the sample into the contact position. The SEPAEARION indicator light will be off and the CONTACT light will illuminate.
10. Select an exposure mode.
11. Standard Mode (ST)

    SOFT CONTACT: This brings the substrate into contact with the mask using the only pressure applied from the contact lever.

    HARD CONTACT: Using Nitrogen to press substrate again the mask. Vacuum under the wafer is OFF.

    High Precision Mode (HP)

    Make the smallest gap between the mask and substrate. So vacuum pump the space between mask and substrate, but vacuum under the wafer is OFF.

12. Set up the desired exposure time. Exposure time=exposure dosage/UV intensity. Exposure dosage is in mJ/cm^2 and the UV intensity is in mW/cm^2. Press the EXPOSURE button on the control panel, the vacuum light will turn off and the mirror moves forward to expose the sample. Do not see the UV light.
13. Move the Contact Lever clockwise to the retracted position when the exposure is done.
14. Remove the sample and take away the mask from the mask aligner. First loosen the knobs on the front and slide the mask holder to the left. Place the mask holders upside down and then press the VACUUM MASK button.
15. Turn off the microscope power supply. Turn off the Mask Aligner by pressing the red POWER on the front control panel. Turn off the lamp controller and vacuum pump.

Figure C.2 Karl Suss MJB3 Mask Aligner.

Magnets at the National High Magnetic Field Laboratory

Figure C.3 Left is 18/20 Tesla General Purpose Superconducting Magnet. Right is 31 Tesla, 50 mm Bore Magnet (Cell 9), the magnetic field in the figure is 28.5T.

The operation procedures of SCM2 and Cell 9 include:

1. Mount the sample to the sample holder. Connect the Probe Sensor Cable to probe temperature controller.
2. Slide load lock all the way down on probe and attach clamps. Move the probe carefully and mount it on gate value and tighten the KF-50 clamp.
3. Connect Turbo Pump out Line to the Probe Load Lock Pump Out Port and tighten the clamp. Open Load Lock Valve and Sliding Seal Valve. When ready, open Pump Valve and turn on Turbo Pump.
4. After the pressure reaches 5×10^{-3} *mbar*, close the Load Lock Valve.
5. Open Gate Valve to load the probe. Make sure the Load Lock Valve is closed.
6. Set the Sorb temperature to 25 K and choose appropriate heater range.

7. Hold the probe and loosen probe clamp to lower the probe slightly. Monitor the cooling rate on the Lakeshore 336 Temperature Controller. Loading the probe too quickly will cause liquid Helium boiling off from the bath.
8. Watch the temperature controller. When output channel D reaches about 4 K, the probe can be lowered again. But the temperature of channel D should start to increase when keep loading, because the probe is passing through the Sorb region located inside the insert, which is at 25 K.
9. Keep lowering the probe until the temperature starts to decrease, stop and tighten the clamp. Wait 10 min to cool down.
10. Hold the probe, remove the clamps and insert the probe all the way slightly. Watch the 1 K Pot temperature and keep it below 1.75 K.
11. Close sliding Seal Valve and Turbo Pump Valve, turn off the turbo pump. Now the sample loading is completed.
12. Condense He^3. Change Sorb temperature from 25 K to 45 K on the temperature controller. Set the heater range as High. Make sure the 1k Pot temperature less than 1.5 K in order to condense Helium. Wait 1 hour for Sorb regeneration.
13. Change Sorb Temperature to desired temperature to get the corresponding probe temperature. For example, Sorb temperature at 2 K gives around 250 *m*K probe temperature.
14. Connect the lock-in amplifiers (SR 350) to the sample. Set up the input voltage and frequency. Start the measurement.
15. Open the NML Data Acquisition software to take data and control magnetic field. For the superconductive magnet SCM2, choose the sweep rate 0.3 T/min

and the magnetic field limit as 18 T. For the 31 Tesla, 50 mm Bore Magnet (Cell 9) which is a resistive magnet, the sweeping rate can be 2 T/min.